Master thesis in Physics

The Influence of Source Extent in EEG/MEG Source Reconstruction of Visually Evoked Responses

Marlene Kallaß
April 2025

Supervised by

PD. Dr. Svetlana Gurevich
Prof. Dr. Carsten Wolters

Acknowledgements

I would like to thank everyone who contributed to and supported me throughout this thesis, especially

- Prof. Dr. Carsten Wolters for the opportunity to work in his group, for his academic guidance and supervision of the thesis.
- PD. Dr. Svetlana Gurevich and Dr. Oliver Kamps for their supervision from the physics department, making it possible for me to write my thesis in an interdisciplinary field.
- Prof. Dr. Sampsa Pursiainen for his time and expertise, and the opportunity to contribute to Zeffiro Interface.
- IBB colleagues, especially Malte Höltershinken and Dr. Tim Erdbrügger for all their help with scientific and software-related questions, Karin Wilken, Ute Trompeter and Hildegard Deitermann for organizing and conducting the measurements, and Andreas Wollbrink for his technical support.
- My family for all of their support throughout my studies.
- Dr. Ravjot Singh Kohli and Ole Körner for proofreading.
- My friends for making every lunch at the Mensa something to look forward to.

This work was supported by DAAD project 57663920, by ERA PerMed as project ERAPERMED2020-227, PerEpi (Bundesministerium für Gesundheit (BMG), project ZMI1-2521FSB006; Academy of Finland (AoF), decision 344712) and by the Deutsche Forschungsgemeinschaft (DFG), project WO1425/10-1 and WO1425/10-2.

I am also grateful to have received financial and ideational support through a scholarship from the German National Academic Foundation (Studienstiftung des deutschen Volkes).

Declaration of Academic Integrity

I hereby confirm that this thesis, entitled "The Influence of Source Extent in EEG/MEG Source Reconstruction of Visually Evoked Responses", is solely my own work and that I have used no sources or aids other than the ones stated. All passages in my thesis for which other sources, including electronic media and AI tools, have been used, be it direct quotes or content references, have been acknowledged as such and the sources cited. I am aware that plagiarism is considered an act of deception which can result in sanction in accordance with the examination regulations.

I confirm that I am aware that my work may be cross-checked with other texts to identify possible similarities and that it may be stored in a database for this purpose.

I confirm that I have not submitted the following thesis in part or whole as an examination paper before.

April 24, 2025 

Contents

1 Introduction

Electroencephalography (EEG) and magnetoencephalography (MEG) are two powerful, complementary methods in neuroscientific research: By measuring the electric potential at the scalp and the external magnetic field around the head, they enable non-invasive, highly time-resolved study of electric brain activity [25][34]. The scientific field of source analysis deals with computational methods of reconstructing the underlying current density inside the brain which generates a measured EEG or MEG (EMEG) signal. This also finds relevant clinical application, e.g., in the case of medication resistant epilepsy: Here, source reconstruction can help localizing the damaged, epileptically active tissue for surgical removal or other treatment options [5][53].

However, the task of reconstructing a current inside a volume conductor based on the external electromagnetic field is an ill-posed inverse problem, as there are infinite source configurations that can generate the same measurement result [28]. Consequently, inverse methods rely on additional assumptions or constraints in order to obtain a unique solution. These a-priori assumptions can e.g. be based on anatomical knowledge. One assumption can be that the solution should be extremely focal, i.e., the entire electric activity is generated by a single point dipole (dipole scanning technique). This is an appropriate approximation in cases that are not too complex, e.g., if the sources are flat patches as shown by de Munck [44]. It does not accurately describe the reality, as the detected activity, in the case of epilepsy, may be spread over several cm^2 of the brain's surface [41]. Applying dipole scanning for very spatially extended sources can lead to misleading localization results [35]. Conversely, there are inverse methods that implicitly assume spatially extended current density distributions, which lead to blurred solutions even if the underlying source is actually a dipole [23]. A more flexible way to incorporate assumptions like this is provided by hierarchical Bayesian modeling (HBM), where constraints are implemented as prior probability distributions which can be adapted to the data at hand [11].

In the context of spatially extended sources, the visually evoked response (VER) is an especially suitable experimental paradigm. Due to the characteristic structure of the visual cortex, the size of the activated zone in the brain is directly correlated to the area of the eliciting stimulus in the visual field [20]. Thereby, the VER can be used to create real experimental data with sources of varying spatial extent.

This thesis investigates the effect of source extent on the properties of the inverse reconstruction using modern source analysis tools. It will be examined under which circumstances spatially extended sources can cause relevant reconstruction errors, and consequently, whether there is a benefit in decreasing the size of the VER stimulus. This should increase the understanding of possible pitfalls when using the investigated methods in clinical applications, where extended sources are likely. Additionally, for applications involving the VER directly - including further methodological studies as well as calibration procedures - a recommendation for the size of the stimulus will be inferred. To achieve this, the finite element method (FEM) is used to accurately

model the human head, and reconstructions are performed using dipole scanning techniques and the HBM-based iterative alternating sequential (IAS) algorithm. The thesis is divided into a simulation study and a group study using real VER EMEG data.

In the simulation part, synthetic EMEG data is created using models of increasing complexity. Sources with varying extents are placed in three different head models: A spherical model, a simplified FEM model with a homogenized brain compartment, and a more detailed FEM model with realistic cortical surfaces. Two types of synthetic sources are used: First, a geometrically simple case with flat, slightly curved patches, consisting of dipoles with radial orientation. In the more complex case of the realistic FEM model, the dipoles in the patch point perpendicularly to the cortical surface. The findings from the simulations are used to determine appropriate settings for the IAS algorithm, and to contextualize the experimental results.

For the experimental part, pattern-reversal VER stimuli of two different sizes are implemented: A ring segment encompassing the whole lower right quadrant of the visual field, and three smaller stimuli, each one third the area of the full stimulus. EMEG data is recorded for each stimulus in a group of 8 participants. Sources are reconstructed from the measured data using dipole scanning and the IAS algorithm, and differences between results for the four stimuli are analyzed.

2 Physiological Background

2.1 Tissues and Signals of the Brain

In the brain, information propagates in the form of electric signals in-between and inside of neurons. Using EEG and MEG, it is possible to non-invasively gain insight on these processes by measuring the electric potential and magnetic field outside of the head, caused by the current within. This chapter deals with the basic structure of the brain and how neurons generate a measurable EMEG signal, with the fundamentals following the presentation in [34].

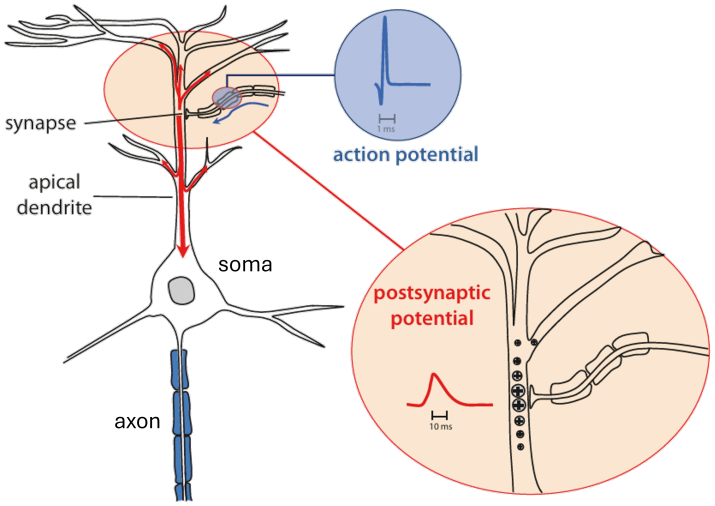

Figure 2.1: A pyramidal cell, consisting of the cell body (soma), axon and dendrites. Axons from other cells connect via the synapse, where the received action potential causes a postsynaptic potential. This leads to current flow along the dendrites [34].

The largest part of the brain, the cerebrum, which is responsible for many cognitive functions, consists of two major tissue types, the grey matter and the white matter. A convoluted outer layer of grey matter with many ridges (gyri) and grooves (sulci) forms the cerebral cortex. It is surrounded by the cerebrospinal fluid (CSF), which allows some movement of the brain within the skull. The cortex contains between 5 and 30 million neurons per cm^2, 85 % of which are the so-called pyramidal cells [14] [17]. Figure 2.1 shows a sketch of a pyramidal cell. The white matter is formed by the neuronal axons, which are long extensions by which the cells send signals to other neurons.

These signals consist of the so-called action potential, a traveling polarization wave which briefly raises the otherwise constant membrane potential by changing the ion concentration difference between the inside and outside of the cell. As this leads to current flows inside the axon in two opposite directions, they cancel out in the far field and therefore do not contribute strongly to the EMEG signal.

The axon connects to the receiving cell via the synapse, where the information is carried on chemically, via neurotransmitters. This causes a local membrane potential change in the new cell, which, depending on the synapse's neurotransmitters, can be positive (excitatory) or negative (inhibitory). The postsynaptic potential leads to a current flow along the dendrites. Signals from different synapses add up and can cause the neuron to send out a new action potential, once a critical excitation threshold is reached. As a dominant part of the dendritic tree of the pyramidal cells points roughly towards the cortical surface (apical dendrites), the parallel currents of neighboring cells add up and are presumed to be the main source for the EMEG signal [62].

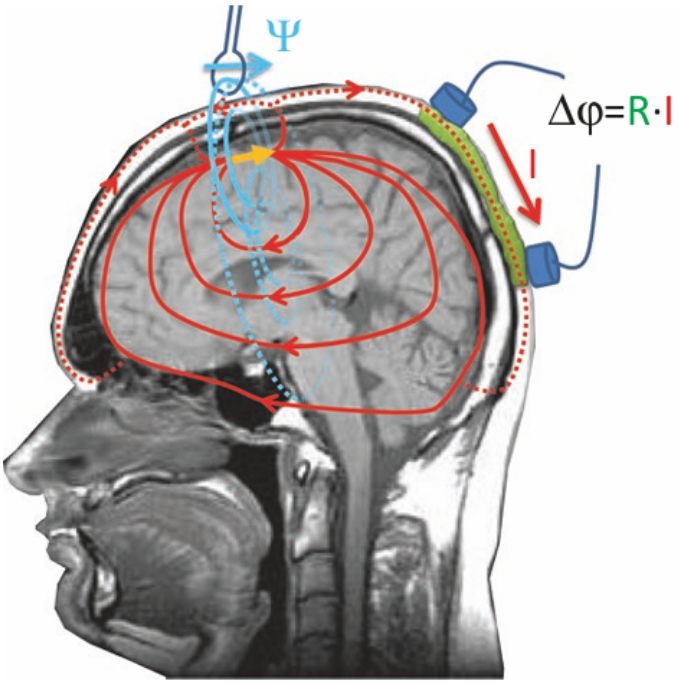

Figure 2.2: Electrodes and magnetometers pick up the electric potential Φ and magnetic flux Ψ caused by the activity in a patch of cortex and the accompanying extracellular return currents [34].

In order to generate a measurable magnetic field outside the head, is is estimated that 10,000-50,000 pyramidal cells must be synchronously active [45]. Theoretically, this would correspond to an area smaller than $1\,\mathrm{mm}^2$ as the minimum area of detectable activity, assuming that all cells within that area are active and there are no additional canceling effects. Making a realistic estimate is difficult: Typically an area of $40\,\mathrm{mm}^2$ is assumed, but it has also been suggested that at least $4\,\mathrm{cm}^2$ of synchronous epileptic activity might be necessary in order to be detectable [26][41].

Due to charge conservation, the intracellular currents give rise to an extracellular return current, which flows through the entire conductive head and causes measurable potential changes at the scalp that can be picked up by the electrodes of the EEG. The intra- and extracellular currents (see Fig. 2.2) also generate a weak magnetic field, which, in a sufficiently magnetically shielded room, can be picked up by MEG magnetometers.

2.2 Visually Evoked Responses

Evoked responses, often called evoked potentials or fields when measured with either EEG or MEG, refer to signals caused by a specific, controlled sensory stimulation. Besides providing insights on the brain's sensory processing pathways in basic neuroscientific research, they are also useful for validating source reconstruction methods: Neuroanatomical knowledge about which cortical areas are known to respond to the stimulation can serve as an approximate ground truth. The somatosensory evoked response has also been used to calibrate the conductive properties of the head model for EEG analysis, taking advantage of the MEG's lesser sensitivity to tissue conductivity [58].

While for strong signals like an epileptic spike, a single spike might suffice for source analysis [6], evoked responses are generally obscured by random background brain activity and sensor noise. To increase the signal to noise ratio, the stimulus is presented many times (trials), with varying inter-stimulus time differences to avoid habituation, and the trials are averaged [16].

There are several types of stimuli commonly used to elicit the visually evoked response (VER), often involving the sudden appearance, spatial movement or color-inversion of a high-contrast pattern on a screen viewed by the participant [47]. The latter, called the pattern-reversal (PR) VER, is used in this thesis. It consists of a flickering black-and-white checkerboard-type pattern taking up part of the visual field, its size measured in degree visual angle (see Fig. 2.3). The checkerboard PR-VER is well-described with regards to its clinical applications, where deviations from the normal response can serve as diagnostic criteria for certain pathological conditions. For that purpose, it is usually measured using a single electrode at the back of the head (specifically, the occipital midline position, Oz, as defined by the international 10-20 electrode placement standard [4]) with a reference electrode at the frontal midline (Fz).

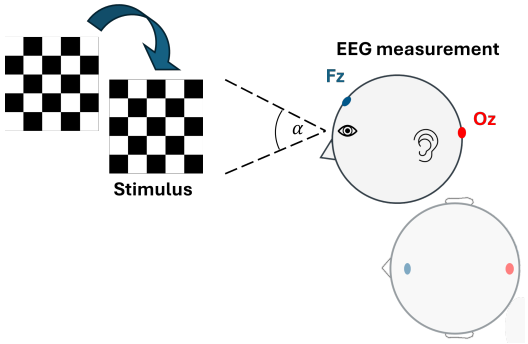

Figure 2.3: Pattern-reversal checkerboard VER, size measured in degree visual angle α and EEG recorded using an electrode at the occipital midline with reference at the frontal midline.

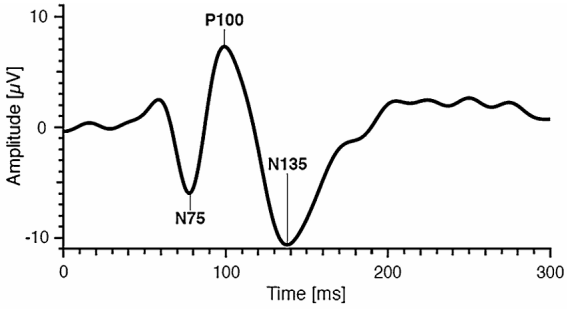

Figure 2.4: Typical post-stimulus time-course of the VER signal at the Oz electrode [47].

Figure 2.4 shows a typical EEG waveform during the post-stimulus time interval measured this way. Three distinct components can be identified, termed the N75, P100 and N135, after their polarities and onset times (latencies). In contrast to the clinical application, in source analysis an array of electrodes over the whole head is used, measuring the topographic potential distribution. Furthermore, while diagnostic criteria are tied to the latency and amplitude of the P100 component, in source analysis the component of interest is often the N75.

Evidently, it takes 75 ms for the signal from the eye to first reach the cortex. Much of this delay (at least 30 ms) is already caused by the limited response time of the photo-receptor cells in the eye's retina [60]. From the eyes, information is transmitted to the brain along the optic nerves. The fibers from both eyes cross over at the optic chiasm, so that information from the left visual field is sent to the right brain hemisphere and vice versa, with a small overlap in the center [31]. The signal reaches the lateral geniculate nucleus, the subcortical relay station between the eye and the visual cortex, after about 40-50 ms (as measured using intracranial depth electrodes [37]). From here it is directly relayed to the primary visual cortex also called V1 or the striate cortex, located at the back of the head (occipital lobe).

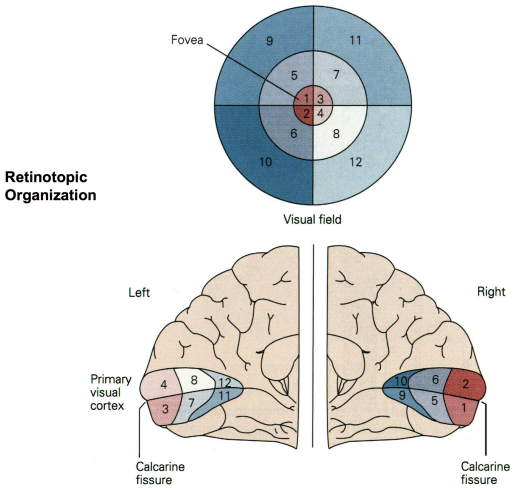

Figure 2.5: Retinotopic organization of the primary visual cortex. The cortex is organized around the calcarine fissure/sulcus, and can be divided into left/right, top/bottom parts. There is a distinct spatial relation between the placement of the stimulus in the visual field and the activated part of the cortex [83].

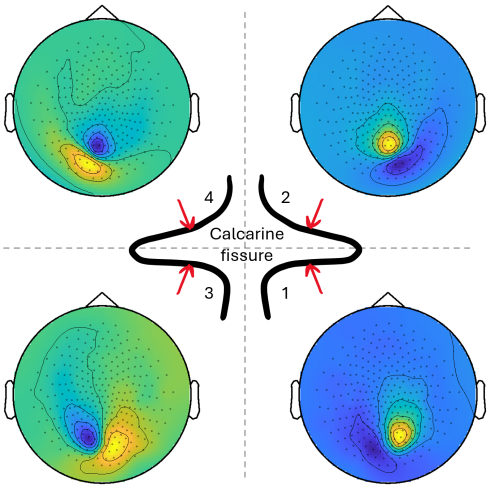

Figure 2.6: Cruciform model of the primary visual cortex (same domain labels as in Fig. 2.5), showing polarity inversion of the MEG topography for stimulation in the four visual quadrants. Data from preliminary tests.

The whole visual cortex is divided into several structural and functional areas, including V1 and extrastriate areas, that form a hierarchical processing system. The V1 is the least specialized but most retinotopic of these regions, meaning there is a clear spatial mapping between the visual field and the cortical area [22]. The upper left part of the visual field is projected to the bottom right part of V1 and vice versa. The central visual field, corresponding to the foveal region of the retina, is mapped nearer

to the skull, and the periphery deeper within the brain. Figure 2.5 shows a sketch of this relation. The strong retinotopy together with the distinct folding of V1 leads to a characteristic polarity inversion of the measured MEG or EEG topography for stimulation constrained to the four visual quadrants. The primary visual cortex is therefore often described in the form of a cruciform model, as shown in Fig. 2.6. With regard to the 75 ms component of the PR-VER, whether (1) V1 is really the only signal contributor, and (2) polarity inversion is a feature unique to V1, is still a subject of debate (see e.g. this discussion between Ales et al. and Kelly et al.: [2], [3], [32], [33]).

In retinotopic mapping studies, which aim to estimate more precisely the spatial relationship between the visual field and the visual cortex, instead of a checkerboard, a round stimulus with a dartboard-like pattern is used. Thereby, the check size and stimulation area is increased when moving further away from the visual focus (increasing eccentricity), to compensate for the cortical magnification factor: The foveal region of the retina, corresponding to approximately the central 2° of the visual field, has a much higher density of photoreceptors than peripheral areas, leading to a larger activated cortical patch for a central stimulus versus an equally sized stimulus in the periphery [27]. This is also visible in Fig. 2.5. Thus, an estimate for the activated area for a certain stimulus needs to take into account its eccentricity. Table 2.1 shows estimates for the cortical magnification factor, i.e., the change in mm of activated cortex length per visual degree in the field of view, for an eccentricity of 3° according to several retinotopic mapping studies. Increasing the size of the stimulus while keeping the eccentricity constant should therefore lead to a corresponding, approximately linear increase of the activated cortical area.

Table 2.1: Estimated cortical magnification values from studies using different methods including functional MRI (fMRI) with a continuously spatially changing stimulus (traveling wave), and source analysis with multifocal VEP (mfVEP), meaning different regions in the visual field are addressed in random order.

Source	**Methods**	**Cortical Magnification at 3° eccentricity (mm/deg)**
Slotnick 2001 [61]	EEG mfVEP source reconstruction n=3	6.2 ± 0.4
Qiu 2006 [52]	fMRI mfVEP n = 5	4.5 ± 0.3
Sereno 1995 [59] (reanalyzed Beard 1997 [7])	fMRI traveling wave VEP n=7	6 ± 1
Horton 1991[30]	Estimate for humans from physiological monkey studies and lesion measurements	4.6

3 The EMEG Forward Problem

Due to the non-uniqueness of the EMEG **inverse problem**, the corresponding **forward problem** needs to be solved first. The forward solution, i.e., the EMEG signal that would originate from a specific source, is computed for a defined space of allowed sources, so that the most suitable solution may be selected from that space. In this section the mathematical formulation of the forward problem is derived from the quasi-static Maxwell equations. Then the analytical solution, which can only be calculated in special geometries, is briefly discussed. For more complex and realistic models of the human head, numerical methods are needed, one of which, the finite element method with St. Venant Source Modeling is used in this thesis and will be described below.

3.1 Derivation from Maxwell's Equations

As the problem in question deals with the propagation of electromagnetic fields the fundamental equations needed are the Maxwell equations. For neural signals, which are low frequency by nature, the quasi-static approximation with the time derivatives of the electric and magnetic fields $\partial_t \boldsymbol{E} = 0$ and $\partial_t \boldsymbol{B} = 0$ is sufficient [26]:

$$\nabla \times \boldsymbol{E} = 0 \tag{3.1}$$
$$\nabla \times \boldsymbol{B} = \mu_0 \boldsymbol{J} \tag{3.2}$$
$$\nabla \cdot \boldsymbol{B} = 0. \tag{3.3}$$

The magnetic permeability of biological tissue is assumed to be identical to the vacuum permeability μ_0, and $\boldsymbol{J}$ denotes the current density.

Equation (3.1) implies that the electric field is rotation-free and can therefore be written as the gradient of a scalar potential:

$$\boldsymbol{E} = -\nabla \Phi. \tag{3.4}$$

The current density $\boldsymbol{J}$ can be divided into the driving intracellular primary current $\boldsymbol{J}^p$ and the secondary volume return current:

$$\boldsymbol{J} = \boldsymbol{J}^p + \sigma \boldsymbol{E} = \boldsymbol{J}^p - \sigma \nabla \Phi, \tag{3.5}$$

where $\sigma \in \mathbb{R}^{3\times 3}$ is a symmetric, positive definite conductivity tensor depending on the local tissue.

Inserting Eq. (3.5) into Eq. (3.2) and taking the divergence yields:

$$\underbrace{\nabla \cdot (\nabla \times \boldsymbol{B})}_{=0} = \mu_0 \nabla \cdot (\boldsymbol{J}^p - \sigma \nabla \Phi). \tag{3.6}$$

This results in the Poisson equation:

$$\nabla \cdot \boldsymbol{J}^p = \nabla \cdot (\sigma \nabla \Phi). \tag{3.7}$$

The EEG forward problem then consists of finding the electric potential $\Phi : \Omega \to \mathbb{R}$ that fulfills Eq. (3.7) in the head domain $\Omega \in \mathbb{R}^3$ under the boundary condition:

$$\boldsymbol{n} \cdot \nabla \Phi = 0 \text{ on } \delta\Omega. \tag{3.8}$$

The boundary condition, with $\boldsymbol{n}$ denoting the unit surface normal of the domain boundary $\delta\Omega$, states that no current flows outside the head.

Due to the distance of the sensors from the source, the primary current density can be approximated as a mathematical point dipole with position $\boldsymbol{r}_0$ and moment $\boldsymbol{d} \in \mathbb{R}^3$, which represents the direction and strength of current flow:

$$\boldsymbol{J}^p = \boldsymbol{d}\delta(\boldsymbol{r}_0), \tag{3.9}$$

where $\delta(\boldsymbol{r}_0)$ denotes the Dirac delta distribution. The magnetic field is calculated using the Biot-Savart law (following directly from Eq. (3.3)):

$$\boldsymbol{B}(\boldsymbol{r}) = \frac{\mu_0}{4\pi} \int_\Omega \boldsymbol{J}(\boldsymbol{r}') \times \frac{\boldsymbol{r} - \boldsymbol{r}'}{\|\boldsymbol{r} - \boldsymbol{r}'\|_2^3} \mathrm{d}^3 r'. \tag{3.10}$$

In the end, rather the magnetic flux through the area of a measurement coil with surface S needs to be calculated:

$$\Psi = \int_S \boldsymbol{B} \mathrm{d}^2 \boldsymbol{s}(\boldsymbol{r}). \tag{3.11}$$

The MEG forward problem can be split into two parts, as the magnetic field can also be split into a primary and secondary component, $\boldsymbol{B} = \boldsymbol{B}^p + \boldsymbol{B}^s$ [57]:

$$\boldsymbol{B}^p(\boldsymbol{r}) = \frac{\mu_0}{4\pi} \boldsymbol{d} \times \frac{\boldsymbol{r} - \boldsymbol{r}_0}{\|\boldsymbol{r} - \boldsymbol{r}_0\|_2^3}, \tag{3.12}$$

$$\boldsymbol{B}^s(\boldsymbol{r}) = -\frac{\mu_0}{4\pi} \int_\Omega \sigma(r') \nabla \Phi(r') \times \frac{\boldsymbol{r} - \boldsymbol{r}'}{\|\boldsymbol{r} - \boldsymbol{r}'\|_2^3} \mathrm{d}^3 r'. \tag{3.13}$$

The primary B field does not depend on the conductivity and can be computed analytically while the secondary part also depends on the electric potential, and usually requires numerical methods.

3.2 Analytical Solution

The solution for the EEG and the MEG forward problems can be calculated analytically in the case of spherical conductors with radially symmetric conductivity profiles. These can serve as adequate approximations for the human head depending on application, with inverse localization errors in the range of 1-4 cm [15][55].

For MEG, Sarvas [57] derived a solution for a spherical model, showing that the external magnetic field is independent of the conductivity values within the sphere. Furthermore, a radially oriented dipole does not produce any external magnetic field. In a real head geometry, the MEG is also less sensitive to quasi-radial source components, an important argument for the complementary nature of EEG and MEG [13].

For EEG, the spherical model is typically made of three (or four) concentric spheres, representing the brain (and sometimes the CSF), skull and scalp with piece-wise constant conductivity values within the respective compartments. In contrast to the MEG, the EEG depends strongly on the conductivity [64]. The forward problem for this multi-layer model can be solved quasi-analytically by a series expansion approximation as derived by de Munck [43].

The analytical solution can be used to validate numerical methods such as the finite element method, which then can be applied to more realistic conductivity profiles.

3.3 Finite Element Method

The finite element method (FEM) is a numerical method that allows solving differential equations like the EEG forward problem in complex geometries. Specifically, it can be used for realistically shaped head models with distinction between white and gray brain matter, which is recommended to avoid both magnitude and topography errors in the forward solution [63].

We want to solve the EEG forward problem for Φ derived in the previous chapter:

$$\begin{aligned} \nabla \cdot (\sigma \nabla \Phi) &= \nabla \cdot \boldsymbol{J}^p && \text{in } \Omega, \\ \boldsymbol{n} \cdot \nabla \Phi &= 0 && \text{on } \delta\Omega. \end{aligned}$$

Firstly, we want to replace this differential formulation by the weak formulation. For this we multiply the equation with a test function w and integrate over the domain Ω.

$$\int_\Omega \nabla \cdot (\sigma \nabla \Phi) w \mathrm{d}^3 r = \int_\Omega \nabla \cdot \boldsymbol{J}^p w \mathrm{d}^3 r. \tag{3.14}$$

We can rewrite the left hand side by applying Green's first identity:

$$\int_\Omega \nabla \cdot (\sigma \nabla \Phi) w \mathrm{d}^3 r = -\int_\Omega \sigma \nabla \Phi \cdot \nabla w \mathrm{d}^3 r + \underbrace{\int_{\delta\Omega} w \sigma \nabla \Phi \mathrm{d}^2 \boldsymbol{s}(\boldsymbol{r})}_{=0} \tag{3.15}$$

The surface integral vanishes due to the boundary condition. This yields the weak formulation of the forward problem:

$$\int_\Omega \sigma \nabla \Phi \cdot \nabla w \mathrm{d}^3 r = \int_\Omega \nabla \cdot \boldsymbol{J}^p w \mathrm{d}^3 r. \tag{3.16}$$

The weak formulation no longer requires Φ to be classically differentiable with continuous second derivatives, as the strong formulation of the differential equation does. It only requires Φ and w to have square-integrable weak derivatives. $\nabla\Phi$ is a weak derivative of Φ if for any v, which is a smooth test function vanishing on the domain boundary, Eq. (3.17) is fulfilled.

$$\int_\Omega \Phi \nabla v \mathrm{d}^3 r = -\int_\Omega \nabla \Phi v \mathrm{d}^3 r. \tag{3.17}$$

To obtain a unique solution, we also require

$$\int_\Omega \Phi \mathrm{d}^3 r = 0, \tag{3.18}$$

as the electric potential is only defined up to a constant. Together this means the solution and test functions are functions in the Sobolev space with zero mean defined in the domain Ω, denoted as $H^1_*(\Omega)$. We can now translate this into a more general form. Let $a(u, w) : H^1_* \times H^1_* \to \mathbb{R}$ be a bilinear form corresponding to the left hand side of Eq. (3.17) and $l(w) : H^1_* \to \mathbb{R}$ a linear functional corresponding to the right hand side. A function $u \in H^1_*$ (corresponding to Φ) is called a weak solution if it fulfills:

$$a(u, w) = l(w) \text{ for all } w \in H^1_*. \tag{3.19}$$

According to the Lax-Milgram theorem, there exists a unique solution to Eq. (3.19)[46][65]. It can not be directly calculated as H^1_* is infinite dimensional. However, according to the Lemma of Céa, in an appropriately chosen finite dimensional subspace $V_h \subset H^1_*$, there exists a $u_h \in V_h$ that can provide a good approximation for u:

$$a(u_h, w_h) = l(w_h) \text{ for all } w_h \in V_h. \tag{3.20}$$

Therefore, in FEM, the domain Ω is split into subdomains, typically hexa- or tetrahedral elements of a mesh, and V_h is defined as the space of functions that have a simple structure on every subdomain. As V_h is finite, it has a basis $\{\phi_1, ..., \phi_n\}$ with n being the number of mesh nodes/vertices:

$$a(u_h, \phi_i) = l(\phi_i) \text{ for } 1 \leq i \leq n. \tag{3.21}$$

The basis functions are piece-wise polynomials, where a ϕ_i associated with the ith node is linear between mesh nodes belonging to the same element, and zero at all other nodes of the mesh and on all other elements. Figure 3.1 visualizes the basis functions for a triangular mesh.

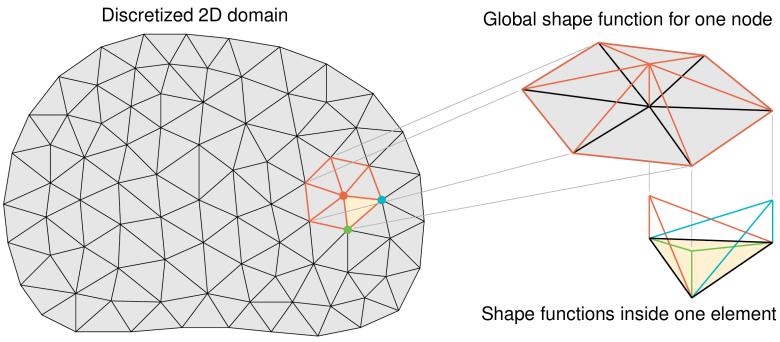

Figure 3.1: Shape functions in a triangular finite element mesh [82].

The solution u_h can be written in terms of the basis functions,

$$u_h = \sum_{j=1}^{n} x_j \phi_j, \tag{3.22}$$

so that the problem becomes:

$$\sum_{j=1}^{n} a(\phi_j, \phi_i) x_j = l(\phi_i) \text{ for } 1 \leq i \leq n. \tag{3.23}$$

In defining the so-called stiffness matrix $(A)_{ij} = a(\phi_j, \phi_i)$ and the vector $(\boldsymbol{b})_i = l(\phi_i)$ we obtain the linear equation system:

$$A\boldsymbol{x} = \boldsymbol{b}. \tag{3.24}$$

A FEM solver algorithm now needs to assemble A for the mesh and solve for $\boldsymbol{x}$. This has to be done for each $\boldsymbol{b}$, i.e., for each source $\boldsymbol{J}^p$. The measured potential y_h of an EEG electrode at position $\boldsymbol{r}$ is obtained by

$$y_h(\boldsymbol{r}) = u(\boldsymbol{r}) - u(\boldsymbol{r}'), \tag{3.25}$$

with a reference at $\boldsymbol{r}'$. As the source space usually contains tens of thousands of sources, it is more efficient to use a computational approach that requires solving the system once for each sensor rather than once for each source. This is the transfer matrix approach [66]. We can rewrite Eq. (3.25) using Eq. (3.22):

$$\begin{aligned} y_h(\boldsymbol{r}) &= \sum_{j=1}^{n} x_j (\phi_j(\boldsymbol{r}) - \phi_j(\boldsymbol{r}')) \\ &= x \cdot \underbrace{\begin{bmatrix} \phi_1(\boldsymbol{r}) - \phi_1(\boldsymbol{r}') \\ \vdots \\ \phi_n(\boldsymbol{r}) - \phi_n(\boldsymbol{r}') \end{bmatrix}}_{= \boldsymbol{c}} \end{aligned} \tag{3.26}$$

An analogous sensor vector $\boldsymbol{c}$ can be defined for the MEG using the Biot-Savart law. Inserting Eq. (3.24) in Eq. (3.26) yields:

$$y_h(\boldsymbol{r}) = \boldsymbol{c}^\top \boldsymbol{x} = \boldsymbol{c}^\top A^{-1} \boldsymbol{b} = T\boldsymbol{b}, \tag{3.27}$$

The transfer matrix T can be calculated, exploiting that A is symmetric, by:

$$AT^\top = \boldsymbol{c}. \tag{3.28}$$

Therefore, a solver needs to first assemble A for the given forward model and then solve Eq. (3.28) for each sensor. In order to obtain y_h, we need to calculate $\boldsymbol{b}$, which requires a suitable source model, described below.

3.4 Venant Source Model

When using FEM, the right hand term of the forward problem, which is the source term $\boldsymbol{b}$, can not be directly calculated from our definition of $\boldsymbol{J}^p$ as a point dipole:

$$\nabla \cdot \boldsymbol{J}^p = \nabla \cdot (\boldsymbol{d}\delta(\boldsymbol{r}_0)).$$

In the FEM framework, we require that this term can be modeled by basis functions ϕ_i, so that:

$$\nabla \cdot \boldsymbol{J}^p \approx \sum_{i=1}^{n} x_i \phi_i. \tag{3.29}$$

This is problematic because the basis functions are smooth and piece-wise continuous while $\delta(\boldsymbol{r}_0)$ has a singularity at $\boldsymbol{r}_0$.

There are several ways to treat the singularity mathematically, one of which is the here utilized St. Venant or blurred dipole approach [9][67]: Following the principle of St. Venant, in the far field the dipole can be approximated by Eq. (3.30), using several appropriately scaled monopoles q_i located at $\boldsymbol{r}_i \in \Omega, i \in \{1, \ldots, m\}$. This is a well-established method, though newer techniques, like the local subtraction approach, can potentially achieve higher accuracy [29].

$$\nabla \cdot \boldsymbol{J}^p \approx \sum_{i=1}^{m} q_i \delta_{\vec{r}_i}. \tag{3.30}$$

The monopole positions usually comprise the vertex nearest to the source location and the vertices belonging to the neighboring elements (see Fig. 3.2). To prevent numerical errors, the locations must fulfill the Venant Condition which requires all monopoles to be in the same conductivity layer as the source, which is normally the grey matter [40] [63].

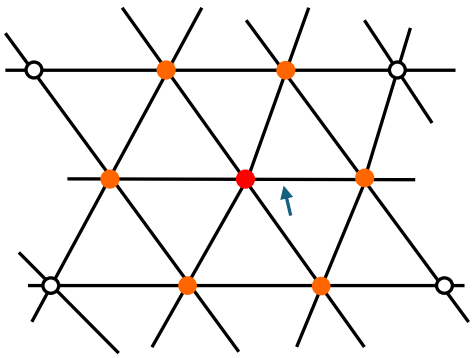

Figure 3.2: Nearest (red) and surrounding (orange) vertices selected as monopole positions to model the dipole (blue).

The monopole strengths are selected in such a way that the dipole moment is reproduced while the net charge remains zero and higher moments are suppressed:

$$\sum_{i=1}^{m} (\boldsymbol{r_i} - \boldsymbol{r}_0) q_i = \boldsymbol{d}. \tag{3.31}$$

4 The EMEG Inverse Problem

Once the forward solution is obtained, the inverse problem can be solved. Due to the discrete sampling of the source space and the sensors, the result of the forward computation is the so-called leadfield matrix. For a source at position $\mathbf{r}_j \in \mathbb{R}^3$ with dipole moment $\mathbf{d}_j \in \mathbb{R}^3$, the leadfield $L_j \in \mathbb{R}^{N\times 3}$ is a matrix mapping the source parameters to the measurement vector $\mathbf{y} \in \mathbb{R}^N$:

$$\begin{aligned} \begin{bmatrix} y_1 \\ \vdots \\ y_N \end{bmatrix} &= \begin{bmatrix} [l_1^x, l_1^y, l_1^z](\mathbf{r}_j) \\ \vdots \\ [l_N^x, l_N^y, l_N^z](\mathbf{r}_j) \end{bmatrix} \cdot \begin{bmatrix} d_j^x \\ d_j^y \\ d_j^z \end{bmatrix}, \\ \mathbf{y} &= L_j \cdot \mathbf{d}_j. \end{aligned} \tag{4.1}$$

The complete leadfield for the whole source space is the set of leadfields $\bar{L} = \{L_1, ..., L_M\} \in \mathbb{R}^{N\times 3M}$ for M source positions and N sensor positions:

$$\underbrace{\begin{bmatrix} y_1 \\ \vdots \\ y_N \end{bmatrix}}_{\boldsymbol{y}} = \underbrace{\begin{bmatrix} [l_1^x, l_1^y, l_1^z](\mathbf{r}_1) & \cdots & [l_1^x, l_1^y, l_1^z](\mathbf{r}_M) \\ \vdots & \ddots & \vdots \\ [l_N^x, l_N^y, l_N^z](\mathbf{r}_1) & \cdots & [l_N^x, l_N^y, l_N^z](\mathbf{r}_M) \end{bmatrix}}_{\bar{L}} \cdot \underbrace{\begin{bmatrix} \mathbf{d}_1 \\ \vdots \\ \mathbf{d}_M \end{bmatrix}}_{\boldsymbol{D}}. \tag{4.2}$$

Solving the inverse problem consists of finding the $\boldsymbol{D}$ that best explains the data and fulfills some additional constraints which need to be made in order to obtain a unique solution. This requires some form of inversion of the leadfield, which generally is not injective. One option is to only consider the local problem (Eq. (4.1)) individually for each position, as this is overdetermined as long as the number of sensors exceeds the number of dipole moment components. That is the idea of the dipole scan explained in Section 4.1. Alternatively, constraints can be added to the model in the form of priors, and a global current density distribution consisting of a superposition of dipole moments can be reconstructed. One inverse method following this principle is hierarchical Bayesian modeling (HBM), which is explained in Section 4.2.

4.1 Dipole Scanning

In the standard single dipole scan, for each source position the reconstructed dipole moment is defined as:

$$\boldsymbol{d}_{j,\mathrm{rec}} = \underset{\boldsymbol{d}_j \in \mathbb{R}^3}{\operatorname{argmin}} \|\boldsymbol{y} - L_j \boldsymbol{d}_j\|_2^2, \tag{4.3}$$

where $\|\cdot\|_2$ denotes the Euclidean norm (l_2-norm). The reconstructed moment can be obtained by calculating the Moore–Penrose inverse L^+ (also called pseudoinverse) which is a generalization of the matrix inverse, fulfilling $LL^+L = L$. Equation (4.4) then constitutes the best fitting moment for a given dipole position to generate the data $\boldsymbol{y}$.

$$\boldsymbol{d}_{j,rec} = L_j^+ \boldsymbol{y}. \tag{4.4}$$

The moment and a residual error measure is calculated for each position. The dipole scan then consists of finding the position which minimizes the error/maximizes the goodness of fit (GOF):

$$\mathrm{GOF}(\boldsymbol{y}, L_j) = 1 - \frac{\|\boldsymbol{y} - L_j \cdot \boldsymbol{d}_{\mathrm{j,rec}}(\boldsymbol{y}, L_j)\|_2^2}{\|\boldsymbol{y}\|_2^2}. \tag{4.5}$$

The single dipole scan is a simple and, for standard sized source spaces, computationally inexpensive method. It also has the advantage that the global maximum is always found. However, it enforces the assumption that the entire data is generated by a single, very focal source. There are also dipole scanning methods designed to find multiple local peaks of GOF, i.e., multiple sources (e.g. MUSIC, see [42]). For the here investigated N75 component of the visually evoked response, the assumption of a single source is appropriate. This source may however be extended over a larger cortical area, with the single dipole scan ideally yielding the approximate location of the distribution's center.

While in the standard dipole scan, L_j refers to a leadfield for a single position in the source space, the mathematical principle works with any subset of $\bar{L}$, as long as the problem remains overdetermined (number of dipole moment components < number of sensors). Based on this idea, a method to reconstruct an extended source using dipole scanning will be introduced in Section 5.4.

4.2 Hierarchical Bayesian Modeling

The inverse problem can be reformulated in the framework of Bayesian statistics. If $\boldsymbol{y}$ is a vector of measurements, $\boldsymbol{D}$ are the parameters of the model $\mathbb{M}$ (the mapping from the parameters to the measurement, i.e., the leadfield), and $p(a \mid b)$ is the conditional probability density function of a random variable a given b, then Bayes' theorem reads:

$$p(\boldsymbol{D} \mid \boldsymbol{y}, \mathbb{M}) = \frac{p(\boldsymbol{y} \mid \boldsymbol{D}, \mathbb{M}) \cdot p(\boldsymbol{D} \mid \mathbb{M})}{p(\boldsymbol{y} \mid \mathbb{M})}. \tag{4.6}$$

The theorem consists of four terms:

- $p(\boldsymbol{D} \mid \boldsymbol{y}, \mathbb{M})$: Posterior probability density of the parameters given the data and the model. An estimate of $\boldsymbol{D}$ can be inferred from the distribution's mean (expectation value) or maximum (Maximum A-Posteriori/MAP).

- $p(\boldsymbol{D} \mid \mathbb{M})$: Prior probability density of the parameters, encoding assumptions or constrains about their possible values.

- $p(\boldsymbol{y} \mid \boldsymbol{D}, \mathbb{M})$: Likelihood of the parameters, equivalent to the conditional probability density of observing the data given the parameters. The likelihood does not necessarily have a unique maximum, which is why a prior is required.

- $p(\boldsymbol{y} \mid \mathbb{M})$: Model evidence, which is the probability that the data can be described by the model, computed by integrating over all possible parameters. This is a normalization term that will be neglected, as we are just interested in the MAP estimate, not the full posterior distribution.

By the use of priors, the Bayesian method therefore does not explicitly enforce a certain number of sources or source extent as the single dipole scan does. Rather, the probability distribution of source configurations is modified according to the given assumptions.

According to the Central Limit Theorem, the data is assumed to be contaminated by additive Gaussian noise ϵ:

$$\boldsymbol{y} = \bar{L}\boldsymbol{D} + \epsilon. \tag{4.7}$$

The noise follows a multivariate Gaussian distribution with mean μ and covariance matrix Σ_ϵ whose probability density function is defined by:

$$p(\boldsymbol{\epsilon}) = \frac{1}{\sqrt{(2\pi)^k \det(\Sigma_\epsilon)}} \exp\left(-\frac{1}{2}(\epsilon - \mu)^\top \Sigma_\epsilon^{-1}(\epsilon - \mu)\right). \tag{4.8}$$

We assume the mean $\mu = 0$ and $\Sigma_\epsilon = \sigma^2 I$, i.e., an independent and identically distributed noise model with known variance σ^2.

From Eq. (4.7) and Eq. (4.8) follows that the likelihood is also a multivariate Gaussian distribution with mean $\bar{L}\boldsymbol{D}$, given by:

$$p(\boldsymbol{y} \mid \boldsymbol{D}) \propto \exp\left(-\frac{1}{2\sigma^2}\|\boldsymbol{y} - \bar{L}\boldsymbol{D}\|_2^2\right). \tag{4.9}$$

If the prior $p(\boldsymbol{D})$ is also Gaussian, then so will be the posterior. Such a prior with zero mean and small variances constitutes a shrinkage prior (Eq. (4.10)), representing the belief that source strengths should be zero unless strong evidence in the data suggests otherwise. The prior variance vector $\boldsymbol{\theta} \in \mathbb{R}^{3M}$ quantifies our belief in this assumption; the larger the variance, the lesser is the influence of the prior on the posterior probability density.

$$p(\boldsymbol{D} \mid \boldsymbol{\theta}) \propto \exp\left(-\frac{1}{2}\boldsymbol{D}^\top \Sigma_\theta^{-1} \boldsymbol{D}\right). \tag{4.10}$$

If Σ_ϵ and $\Sigma_\theta = \mathrm{diag}(\theta_1, ..., \theta_{3M})$ are known and fixed, one can formulate the Maximum-a-Posteriori (MAP) solution as:

$$\langle \boldsymbol{D} \rangle_{\mathrm{post}} = \underset{\boldsymbol{D}}{\mathrm{argmax}} \left(\log\left(p(\boldsymbol{D} \mid \boldsymbol{y})\right)\right). \tag{4.11}$$

This constitutes a minimization of the difference between the data and $\bar{L}\boldsymbol{D}$, penalized by the model term, which corresponds to a Σ_θ-weighted l_2-norm of the solution $\boldsymbol{D}$. The solution to Eq. (4.11) is

$$\langle \boldsymbol{D} \rangle_{\mathrm{post}} = \Sigma_\theta \bar{L}^\top \left(\bar{L}\Sigma_\theta \bar{L}^\top + \Sigma_\epsilon\right)^{-1} \boldsymbol{y}. \tag{4.12}$$

If the noise covariance matrices are both scaled identity matrices this simplifies to

$$\langle \boldsymbol{D} \rangle_{\mathrm{post}} = \bar{L}^\top \left(\bar{L}\bar{L}^\top + \lambda I\right)^{-1} \boldsymbol{y}, \tag{4.13}$$

which is a well known formulation of Tikhonov-regularized minimum norm estimation, where a parameter λ can be adjusted in order to regularize the solution. However, selecting an appropriate degree of regularization may be challenging. In HBM, this problem is addressed by modeling the prior variances as random variables as well, which can be estimated empirically from the data. The variance vector is therefore equipped itself with a so-called hyperprior $p(\boldsymbol{\theta})$:

$$p(\boldsymbol{\theta} \mid \boldsymbol{y}) \propto p(\boldsymbol{y} \mid \boldsymbol{\theta}) p(\boldsymbol{\theta}). \tag{4.14}$$

We want the hyperprior over the variances to favor small values while permitting larger outliers, which should allow for a focal solution, with most source strengths being zero and a few strong sources. One distribution that meets this requirement is the inverse gamma function shown in Fig. 4.1. It is a heavy-tailed distribution governed by two parameters, the shape parameter $\alpha \in \mathbb{R}_{>0}$ and scale parameter $\beta \in \mathbb{R}_{>0}$:

$$p(\boldsymbol{\theta}) \propto \prod_{i=1}^{3M} \theta_i^{-\alpha-1} \exp\left(-\frac{\beta}{\theta_i}\right). \tag{4.15}$$

The scale parameter primarily effects the spread or width of the distribution and the shape parameter steers the rate of decay of the tail [11].

The inverse gamma distribution is often chosen as a hyperprior distribution in HBM, as it is conjugate to the Gaussian likelihood, ensuring that the variance posterior $p(\boldsymbol{\theta} \mid \boldsymbol{y})$ is also inverse gamma. This can make computations more efficient in methods where the whole posterior distribution is estimated, like sampling techniques. These techniques can also be used to approximate appropriate seed points for faster optimization methods like the IAS algorithm (see Section 5.5) [39]. In the case of this algorithm, the inverse gamma distribution as hyperprior is not a requirement.

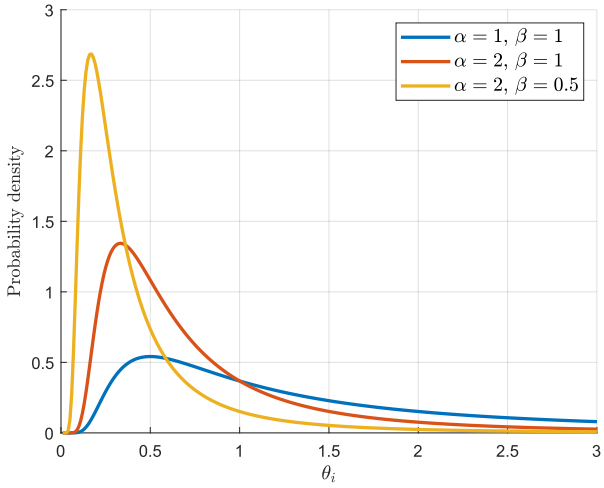

Figure 4.1: Inverse gamma probability density function for different shape and scale parameters.

5 Experimental and Computational Methods

EEG and MEG data of 8 subjects was recorded at the Institute for Biomagnetism and Biosignalanalysis (IBB), University of Münster. Additionally, Magnetic Resonance Imaging (MRI) scans of all subjects were acquired in order to create realistic head models. A range of different software was used to process the data and perform forward and inverse computations. Most of this process was done using the institute-developed pipeline for EMEG source analysis [70]. The pipeline is implemented in Matlab (The MathWorks, Inc., Natick, Massachusetts, USA) and calls upon several freely available toolkits and software libraries, each developed for applications in neuroscientific analysis with strengths in different domains. Additionally, results from the pipeline were imported into the Matlab toolbox Zeffiro Interface, developed at Tampere University, which contains the IAS algorithm [73]. The creation of synthetic data and evaluation of the results was also performed in Matlab.

5.1 Experimental EMEG Data

5.1.1 Participants

The group study included 4 male and 4 female participants, aged 21-29 (mean 23 ± 2). The participation in the study was voluntary and ethical clearance given by the ethics committee of the Ärztekammer Westfalen-Lippe (Ref No 2021-290-f-S, amendment from December 7, 2023). Subjects either had normal or corrected eyesight using contact lenses or provided MEG-compatible glasses. Stimulation occurred binocularly.

5.1.2 Visual Stimuli

A pattern-reversal dartboard stimulus as explained in Section 2.2 was implemented using the Matlab Toolbox Psychophysics [69], based on existing code for a checkerboard stimulus [56].

Previous investigations have shown that for the upper half of the visual field, one of the two poles of the MEG topography lies partially outside of the scope of the MEG sensor array, potentially negatively affecting localization [56]. Therefore, the lower right quadrant was chosen for stimulation in this thesis.

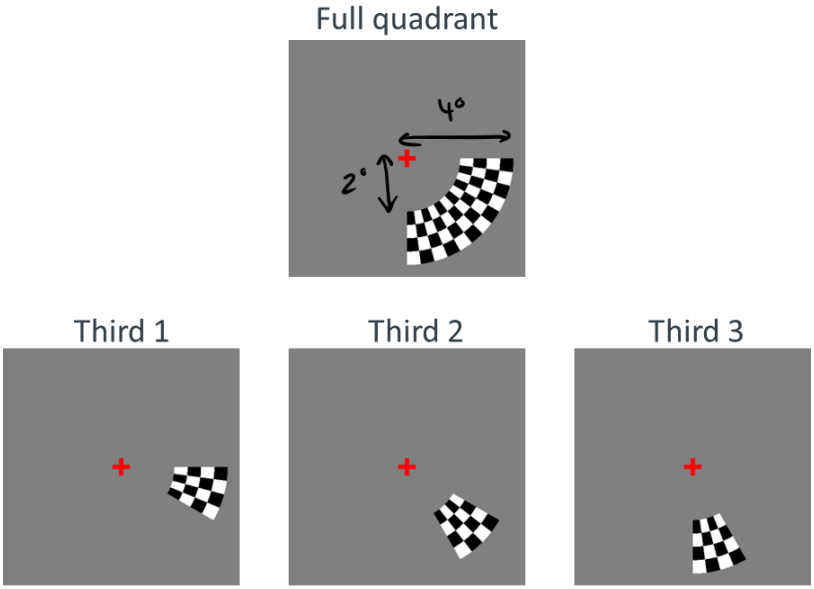

Figure 5.1: Dartboard pattern-reversal stimuli used in the VER experiments.

Figure 5.1 shows the four different stimuli that were implemented. Stimuli are presented on a gray background with a red cross in the center on which participants were told to focus. The first stimulus consists of a ring segment extending 2° to 4° visual angle from the fixation cross and taking up the full lower quadrant. It contains 4×12 black and white checks with length (in radial direction) of 0.5° and width (in tangential direction) between 0.26 and 0.52°, depending on eccentricity. This lies within the range for check sizes (0.25-1°) specified in the International Society for Clinical Electrophysiology of Vision (ISCEV) standard [47]. The three additional stimuli each consist of a 30° segment of the full quadrant stimulus.

In small-angle approximation, 1° visual angle corresponds linearly to a constant distance on the stimulus presentation screen, so that the area of a small segment can be calculated as $\frac{1}{12}\pi((4°)^2 - (2°)^2) = \pi^{°^2}$. Assuming a circular cortical activation patch, which may not be the reality, but can be better compared to the simulations (Section 5.3), and taking the values for cortical magnification at eccentricity 3° from Section 2.2, this would correspond to an activation with a radius between 4.2 and 7 mm. The full stimulus would then activate three times the area, i.e., a radius between 7.2 and 12 mm.

In accordance with the ISCEV standard, the mean pattern switching rate was set to 2 reversals per second, with interstimuli times varying randomly between 400 ms and 600 ms. A measurement consisted of 1000 pattern reversals and lasted about 500 s (8:20 min). The time points of the pattern reversals were recorded using a trigger signal sent to the acquisition software.

5.1.3 EMEG Measurement

EEG data was recorded using a cap of 54, 56 or 58 (depending on head size) AgCl sintered electrodes (EASYCAP, Herrsching, Germany), attached to the scalp using a conductive paste. Four additional electrodes were placed around the eye for electrooculography (EOG) to measure eye-blinks. The head shape and relative positions of the electrodes were measured using a Polhemus tracking system (FASTRAK, Polhemus Incorporated, Colchester USA). MEG data was recorded simultaneously with EEG using 275 axial gradiometers (OMEGA2005, VSM MedTech Ltd.,Vancouver, Canada).

An axial gradiometer consists of two superconducting quantum interference device (SQUID) sensors with a few cm distance, arranged approximately perpendicularly to the scalp. Thus the difference in magnetic flux is measured and noise from spatially constant background fields cancels out.

The sampling rate was 600 Hz. Subject movement during recording was monitored using head localization coils and position deviations over 5 mm noted in the measurement protocol. The visual stimulus was presented by light projecting the computer generated images onto a screen at 92 cm distance from subjects. The normal room lighting of the MEG chamber remained turned on during the visual experiments.

A total measurement run consisted of the presentation of six different visual stimuli in randomized order, of which four were used in this thesis and two belonged to a different study. With a measurement time of on average 8:20 min per stimulus and variable resting times for each participant, the total measurement time was about 1 hour per participant.

5.1.4 Processing of EMEG Data

Data processing was performed using FieldTrip (Donders Institute for Brain, Cognition and Behaviour, Radboud University, the Netherlands) [77].

The frequency range of the pattern-reversal VER lies within 3-30 Hz [8]. Guidelines recommend a bandpass filter in the range of about 1-100 Hz [47]. However these recommendations are for clinical applications, where the main concern in choosing a filter range is not to distort the latency and amplitude of the P100 component. For VER source localization, there are no guidelines, but choosing a lower lowpass filter has shown good signal-to-noise ratio for the 75 ms component [12][19][56]. Therefore, the data was filtered using a 1-40 Hz Hann window bandpass filter. This also removes power line noise at 50 Hz. Additionally a baseline correction with the baseline calculated from the mean of the whole data set per channel was applied.

The data was then segmented into the individual trials, each consisting of the time interval from 100 ms pre-stimulus to 200 ms post-stimulus. Trials containing eye-blinks were automatically detected and removed by FieldTrip based on the z-score (number of standard deviations away from the overall mean) of the EOG signal. The next step was to homogenize the data by removing bad channels and trials. Especially for the

EEG, the caps contained some defect electrodes and typically some that were not properly attached to the scalp, e.g., due to hair. The number of remaining functional EEG channels varies between subjects, ranging from 43 to 51 (with the exception of subject 7, see Section 7.1). No MEG channels were removed as part of the normal preprocessing procedure, however later analysis will show the benefit of excluding frontal magnetometers (see Section 7.1).

A statistic over all trials and channels was visually inspected and channels, single trials or whole time segments of trials that strayed strongly from the distribution are manually removed. This was done largely based on the variance, the range (minimum and maximum value), and the z-score. Figure 5.2 shows such a distribution for a MEG measurement with an artifact just after 7 minutes, coinciding with a measured movement of the participant at that time point. The trials containing the artifact were removed. The remaining trials (about 900-950) were then averaged. A second baseline correction was applied with the mean calculated from the prestimulus interval. This is a necessary correction of the first baseline correction, which smears signal components into the prestimulus interval, as it is computed over the whole data set.

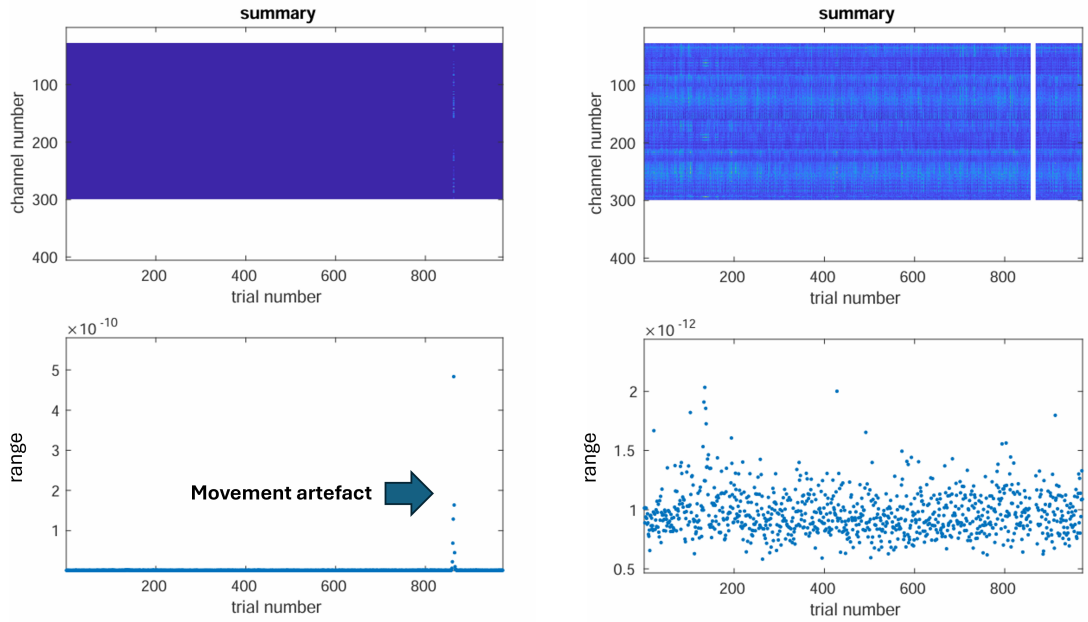

Figure 5.2: MEG measurement with an artifact caused by participant movement (left). Displayed is the signal range of each trial, top: shown per channel, bottom: averaged over channels. Right: The trials containing the artefact are removed.

The individual time point of the N75 component was determined visually from the EEG and MEG time courses over all sensors. Signal-to-noise ratio (SNR) is calculated by dividing the global mean field power (GMFP) of the N75 peak by the mean GMFP during the time interval from -50 ms to 0 ms. The GMFP is a measure of global variance across sensors, estimating the differences between signal amplitudes at each sensor y_i to the mean signal amplitude $\bar{y}$:

$$\mathrm{GMFP}(t) = \sqrt{\frac{1}{N}\sum_{i=1}^{N}(y_i(t) - \bar{y})}. \tag{5.1}$$

5.2 Forward Modeling

5.2.1 MRI Acquisition

MRI data was recorded for all participants at IBB using a 3 T Siemens MAGNETOM Prisma scanner (Siemens Healthineers, Erlangen, Germany). T1-weighted images were acquired using a 3D MP-RAGE sequences with parameters TR = 2300 ms, TE = 3.51 ms, TI = 1100 ms and flip angle = 8°. T2 weighted image were acquired using a 3D spin echo pulse sequence with TR = 3200 ms, TE = 408 ms, flip angle = 120°. The obtained volumetric data has 1 x 1 x 1 mm resolution and 192 x 256 x 256 mm field of view. Prior to measurement, MRI markers containing a Gadolinium-based contrast agent were placed on three distinct physiological landmarks (nasion and the left/right preauricular points, see Fig. 5.3), for later alignment with the EEG sensors.

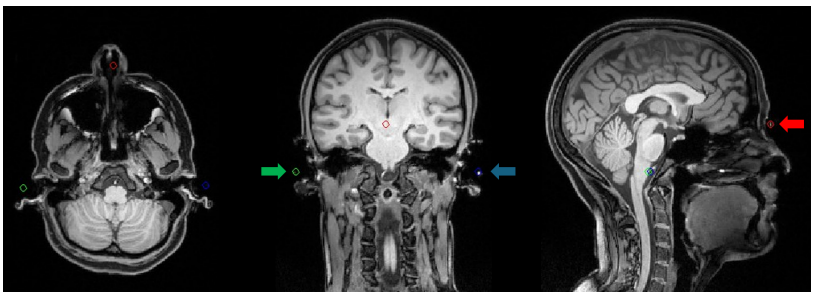

Figure 5.3: Fiducial points: Nasion (red), left/right preauricular (green/blue).

5.2.2 MRI Segmentation

The automatic segmentation process in the analysis pipeline relies on the SPM12 software toolkit (Statistical Parametric Mapping, Functional Imaging Laboratory, Institute of Neurology, University College London, UK) [71] with add-on package CAT12 (Computational Anatomy Toolbox 12, Structural Brain Mapping group, Jena University Hospital, Germany) [72] for advanced segmentation algorithms.

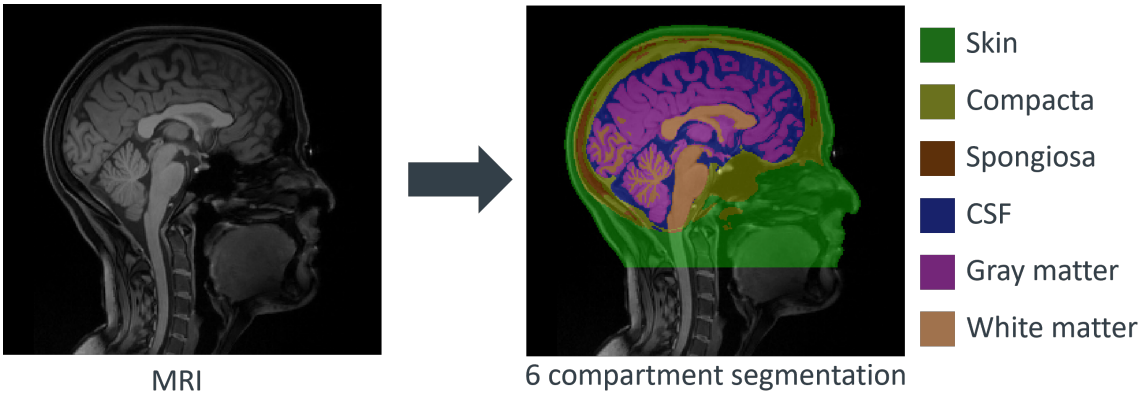

Figure 5.4: MRI segmented into 6 different tissue types.

The T1 and T2 images were denoised using the CAT Spatial-Adaptive Non-Local Means filter, which is a filtering method especially adapted for the spatially-varying noise levels of MRI data [75]. The T1 image was aligned to the T2 image using the FSL tool FLIRT for linear affine brain image registrations (FMRIB Software Library, Functional Magnetic Resonance Imaging of the Brain Analysis Group, Oxford University, UK) [74].

First, independent segmentation masks of the different compartments were created for T1 and T2, making use of the complementary strengths of the two weightings: T1 was used for the segmentation of gray matter and white matter and T2 for the segmentation of the skull into the two bone types, spongiosa, and compacta. Both were used to create individual masks for CSF and the scalp. The skull and scalp masks were manually checked and if required, the segmentation threshold was adjusted. The independent masks were then combined to create the most accurate segmentation by comparing where masks overlap and for example using the T2 skull mask to restrict the area of the T1 brain regions.

This results, as shown in Fig. 5.4, in a segmentation map of the head into six compartments: white matter, gray matter, CSF, spongiosa, compacta and scalp.

5.2.3 Headmodels and Source Spaces

For the evaluation of the real experimental data, it is crucial to reduce the error introduced by inaccurate forward modeling by modeling the head as realistically as possible. However, for synthetic data, where the same model is used for the creation of the data as for the inverse reconstruction, there is no modeling error. Therefore, the simulations were first performed for simplified models with high resolution symmetric source spaces. This enables the investigation of potentially small systemic errors due to source extent effects without taking irregularities caused by the local cortex geometry into account yet.

1) FEM model with 6 compartments

Using the MRI segmentation, a geometry-adapted hexahedral finite element mesh, displayed in Fig. 5.5, was created with SimBio-VGRID [80]. The compartment boundaries of the mesh were refined by shifting nodes close to a tissue boundary onto the boundary [67]. A 2 mm resolution source grid was created with positions restricted to the gray matter and fulfilling the Venant condition.

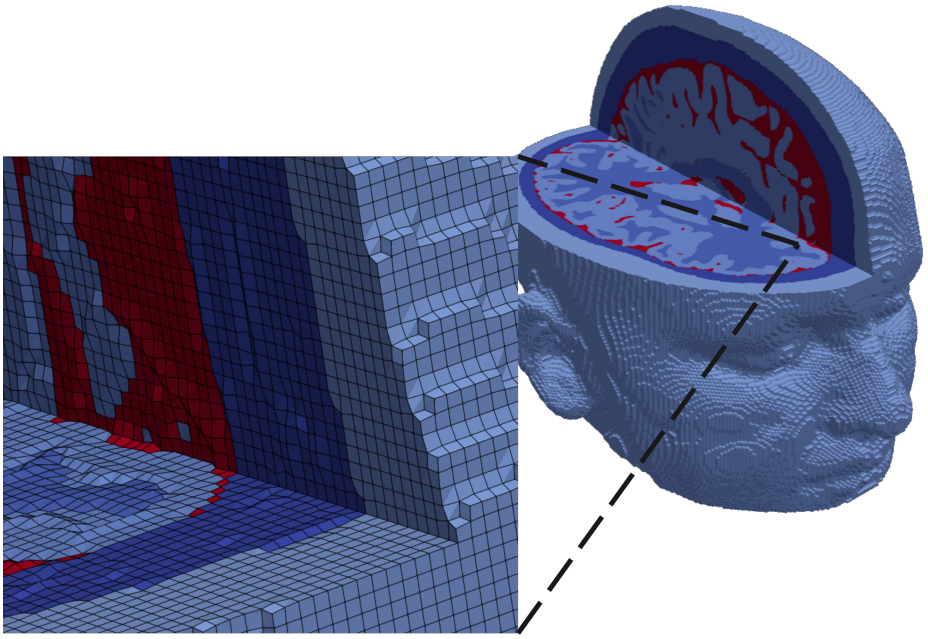

Figure 5.5: Hexahedral mesh with shifted nodes. Figure created using ParaView [68].

For the calculation of the leadfield, the positions of the sensors used in the experimental data need to be transformed into the same coordinate system and fit to the head shape defined by the FEM mesh. For this, the fiducial points visible in the MRI were manually marked, and the head shape measured with Polhemus aligned accordingly. Then the Polhemus points were fitted to the scalp surface of the mesh using an optimization algorithm from the open-source software Brainstorm [81], and the sensor positions were moved accordingly.

From here, the EEG and MEG leadfields were computed using the DUNEuro software library for solving partial differential equations in neuroscience [78]. The conductivity values assigned respectively to scalp, compacta, spongiosa, CSF, white matter and gray matter were 0.43, 0.0042, 0.0151, 1.79, 0.33, and 0.14 S/m (siemens per meter) based on [1].

2) Analytical 3-compartment sphere

Using FieldTrip, a 3-compartment sphere model consisting of brain, skull, and scalp was fitted to the previously created mesh. A 3-dimensional symmetric source space was constructed in a way that is most suitable for the placements of the synthetic source patches (see Section 5.3). The source space is therefore radially symmetric instead of the typical cubic grid, as sketched in Fig. 5.6. It has a resolution of 1 mm into the depth and a tangential resolution that ranges from 0.6 to 1 mm depending on depth. To create a uniform spherical distribution of source points, the Matlab toolbox Uniform Sphere Sampling was used [79]. Also using FieldTrip, the EEG leadfield was computed analytically.

The sphere model for Subject 1 was used for simulations, additionally for all subjects sphere models were created to define the directions of radial and tangential in the FEM models when describing source orientations and depths.

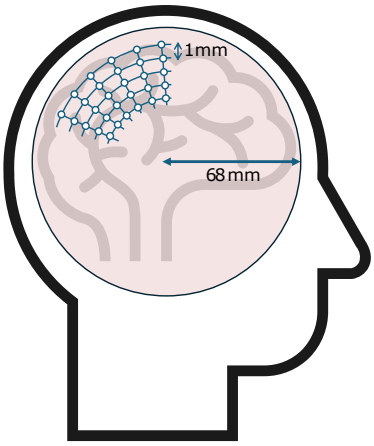

Figure 5.6: Sketch of a spherical headmodel (brain compartment) with a spherically symmetrical source space.

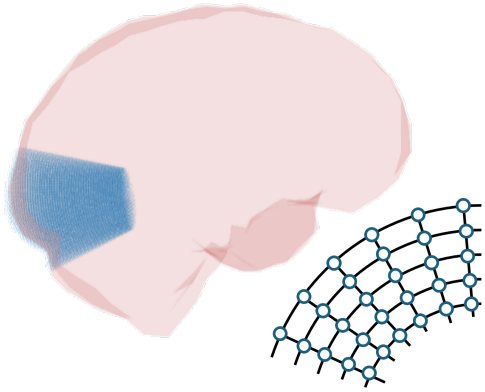

Figure 5.7: Homogeneous brain with spherical source space that is restricted to a part of the brain surrounding the visual cortex.

3) FEM model with homogenized brain

This model is based on the 6-compartment mesh, with the conductivity of gray matter, white matter and CSF set to the same value of 0.33 S/m, creating one homogeneous brain compartment. The source space is not restricted to the cortical surface but rather has the same homogeneous geometry as that of the sphere model, just cut-off at the boundary of the brain. This allows performing the same analysis as in the sphere model, using a realistic head shape but without complicated effects of unsymmetrical patch geometries. The source space was restricted to a part of the brain surrounding the visual cortex to reduce computational burden.

Distinguishing between spongiosa and compacta in the skull layer but not between brain matter and CSF is unusual, because the latter has a much stronger effect on the reconstruction [63]. Here, it was done in order to allow a symmetrical 3-dimensional source space while keeping the rest of the model identical to the already existing full 6-compartment model.

To avoid a so-called inverse crime, for the simulations with the spherical and 4-compartment models, the respective source spaces were subsequently divided into two subspaces: One was used to create the synthetic data, and one as the solution space for the inverse method. Otherwise, if the same source space is used for both forward and inverse calculations, one runs the risk of obtaining overly optimistic results.

5.3 Synthetic EMEG Data

Synthetic data was created using the previously obtained leadfields, and calculating the forward solution for source patches placed in the region of the visual cortex. A patch consists of many dipoles with equal amplitude but variable orientation. The forward signals originating from each dipole within the patch were added together and (optionally) Gaussian noise was added to generate the synthetic data.

Two different types of patches were implemented:

1) Flat patches with radially oriented dipoles

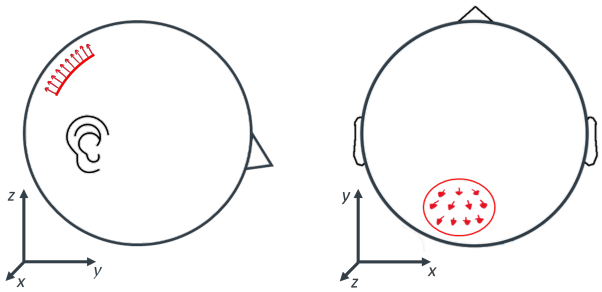

Figure 5.8: Sketch of the newly implemented source patches: The patch is a circular, curved disk consisting of many dipoles each with radial orientation.

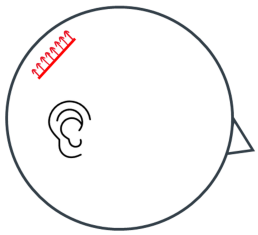

Figure 5.9: Flat patches as implemented by de Munck [43]. The patch is a circular, planar disk and the dipoles are oriented parallel to one another.

These patches, visualized in Fig. 5.8, were used for simulations in the spherical and 4-compartment head model with homogeneous, spherically symmetrical source space. They are circular disks extending tangentially. As opposed to the flat patches used by de Munck in [43] (see Fig. 5.9), these patches are slightly curved following the curvature of the source space. The orientations of the dipoles are normal to the surface of the patch, which, due to the curvature, is exactly the same as each dipole having radial orientation. The patches were placed in a way that they are centered around a position that is not contained in the source space used for the creation of the synthetic

data, but is in the inverse solution source space. Thus, if the center of the patch is correctly reconstructed using a single dipole scan, the localization error can be zero, while still avoiding an inverse crime. Due to the MEG's insensitivity to radial sources, simulations with these patches were only performed for EEG.

2) Ellipsoidal patches with normally oriented dipoles

For the 6-compartment FEM model, the source space is much more irregular, following the individual cortical surface, and has a lower resolution. This means few dipoles are likely to lie perfectly on the surface of a flat patch. Therefore, an ellipsoid-shaped region of interest (ROI) with a thickness of 4 mm in radial direction, and equal axes of variable length in tangential direction was implemented. The orientations of the dipoles in the patch are no longer radial, but normal to the cortical surface. The choice of an ellipsoidal patch was also motivated by the way that extent was measured for the current density reconstruction, for which an ellipsoid was fitted to the distribution (see Section 5.5.2). As the dipoles are known to be normally oriented, this constraint was also imposed for the reconstruction with IAS (see Section 5.5).

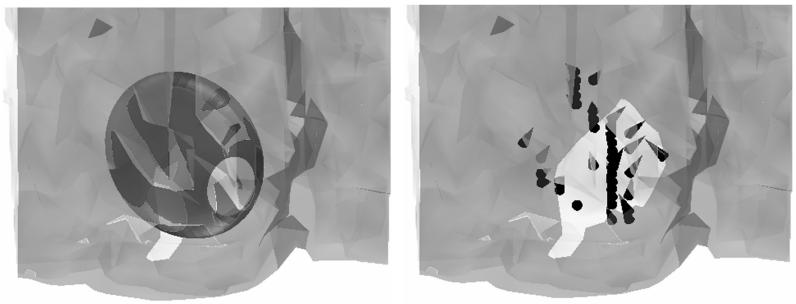

Figure 5.10: Ellipsoidal ROI containing dipoles oriented normal to the cortical surface.

To create the synthetic data in Zeffiro Interface, a new UI tool adapted from the normal synthetic data generation tool for single dipoles was implemented. The tool allows defining one or several ROIs which should contain active dipoles. The ROIs can be spherical or ellipsoidal. One can also choose between dipoles within the ROI having all the same, specified orientation, or automatically take on a cortex-normal orientation. The tool also includes the option to plot the ROIs or the individual dipoles as cones, as shown in Fig. 5.10. It is available at the Zeffiro Interface GitHub repository [1].

[1]The Zeffiro Interface source code including the synthetic source tool can be accessed at: `https://github.com/sampsapursiainen/zeffiro_interface`.

5.4 Patchy Dipole Scan Method

In addition to the standard single dipole scan a "patchy" dipole scan was implemented. As mentioned in Section 4.1, the scanning method also works with larger subsets of the leadfield. Because the shape of the patches used in the simulations is known, it is possible to scan for sources of that same geometry. Therefore, in this technique each subset of $\bar{L}$ consists of leadfields $\{L_1, ...L_n\}$ of dipoles that are considered part of a patch, and the source space is scanned for all possible patch center positions. Equation (5.2) then reconstructs the moments of all dipoles contained in a patch.

$$\begin{bmatrix} d_1^x \\ \vdots \\ d_n^z \end{bmatrix} = \begin{bmatrix} L_1 & \dots & L_n \end{bmatrix}^+ \mathbf{y}. \tag{5.2}$$

However, due to the high resolution of the source space, a patch with a radius of a few mm could potentially consist of hundreds of dipoles. This is not feasible for the dipole scan method, as the number of dipole components is required to be smaller than the number of sensors. For the 59 EEG sensors in the simulation, this means there can not be more that 19 dipoles inside a patch. This can be achieved by decreasing the resolution of the source space. However, that is not necessary. We can still allow every position in the high resolution source space as a potential center of a patch, but construct the patch itself of only a subset of the surrounding points. For symmetry reasons, the positions considered as part of a patch therefore consisted of 7 dipoles for small patches, and 10 dipoles for patches with radius $\geq$6 mm, distributed symmetrically within the patch as shown in Fig. 5.11.

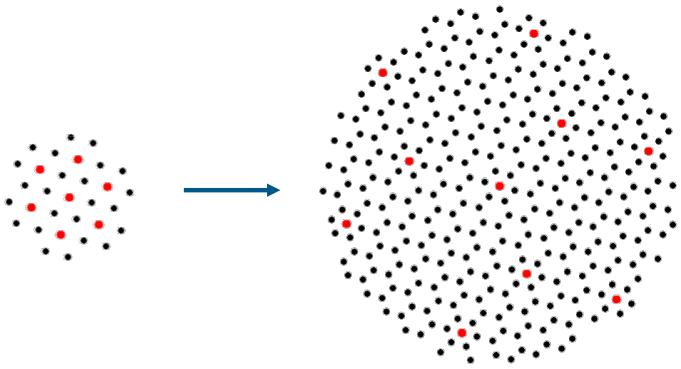

Figure 5.11: Patchy dipole scan: Black are the actual dipole positions inside the patch used for creating the synthetic data, red are the positions considered part of the patch in the scanning method.

5.5 IAS Optimization Algorithm

The iterative alternating sequential (IAS) algorithm as introduced by Calvetti and Somersalo [10] is one of the HBM methods provided in Zeffiro Interface. It is a cyclic optimization algorithm to find the source parameters which maximizes the posterior (MAP estimation).

The algorithm alternately optimizes the source parameters $\boldsymbol{D}$ with the current prior $p(\boldsymbol{D}|\boldsymbol{\theta})$, and then optimizes $\boldsymbol{\theta}$, until a specified iteration number K:

Start by initializing $\theta_i^{[0]}$ as β and set $k = 1$.

For $k = 1, ..., K$ do:

1. Update $\boldsymbol{D}$ by $\boldsymbol{D}^{[k]} = \text{argmax}(p(\boldsymbol{D} \mid \boldsymbol{\theta}^{[k-1]}, \boldsymbol{y}))$

2. Update $\boldsymbol{\theta}$ by $\boldsymbol{\theta}^{[k]} = \text{argmax}(p(\boldsymbol{\theta} \mid \boldsymbol{D}^{[k]}, \boldsymbol{y}))$

The final reconstruction is then given by the last sample $\boldsymbol{D}^{[K]}$. For details see [11].

5.5.1 Parameters and Settings

In Zeffiro Interface, the values for the shape and scale parameters α and β of the hyperprior are not directly chosen, but determined from the specified SNR, the Prior-over-Measurement SNR (PM-SNR) and the tail length. For details on this parametrization see [54].

For experimental data, the SNR needs to be estimated, for simulated data it is simply the SNR that was used to create the data. The PM-SNR constitutes the belief in additional latent noise and scales the SNR with $\text{SNR}_{\text{tot}} = \text{SNR} - \text{PM-SNR}$ (in dB) with $\text{SNR}_{\text{tot}} = \text{dB}(\frac{1}{\sigma_{\text{tot}}})$. As suggested in [54], the PM-SNR was set to 10 dB for simulations, and 20 dB for experimental data to account for additional modeling errors. The number of IAS iterations was set to 5.

The tail length $\text{dB}(\tau)$ is a parameter that primarily influences the shape of the distribution, and indirectly the scale (see Fig. 5.12). The parametrization via the tail length allows adjusting the weight of the tail while automatically taking the noise into account: The shape parameter α is optimized so that the inverse Gamma probability density function evaluated at a point $\theta_{\text{thr}} = \sigma_{\text{tot}}^2 \cdot \tau^2$ matches a threshold value of $2 \cdot 10^{-3} \cdot (\sigma_{\text{tot}}^2 \cdot \tau^2)$. A larger tail length should lead to a higher probability for larger prior variances which in turn allows for a few sources to strongly deviate from the expectation of zero amplitude. By varying the tail length it is therefore possible to bias the reconstruction algorithm towards more focal or more distributed current densities.

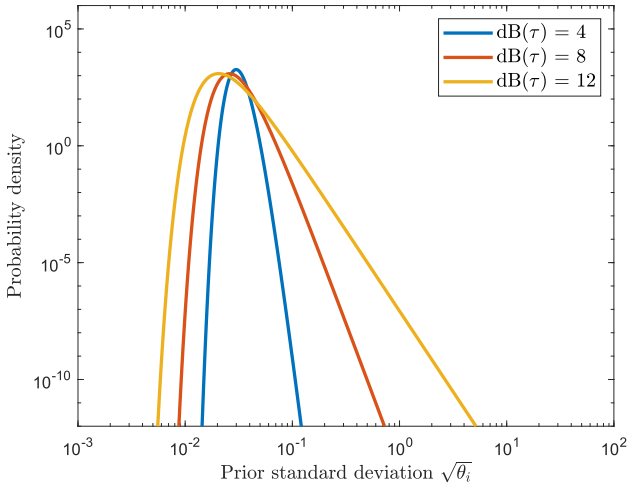

Figure 5.12: Inverse gamma hyperprior for different tail lengths db(τ) with shape and scale parameters: $\alpha = 17.9$, $\beta = 1.7 \cdot 10^{-5}$; $\alpha = 5.1$, $\beta = 4.1 \cdot 10^{-6}$ and $\alpha = 2.5$, $\beta = 1.5 \cdot 10^{-6}$.

The scale parameter is then adapted to the size of the source space $3M$ by

$$\beta = \frac{A^2 \cdot \sigma_{\text{tot}}^2 \cdot (\alpha - 1)}{3M}, \tag{5.3}$$

where the expected source amplitude A is estimated from the leadfield:

$$A = \frac{1}{3M} \sum_{j=1}^{3M} (\max_i \mid \bar{L}_{ij} \mid)^{-\frac{1}{2}}. \tag{5.4}$$

The reconstruction is reweighted in each step using a standardization procedure. As derived in Eq. (4.12), the source parameters in each iteration are:

$$\boldsymbol{D}^{[k]} = W^{[k]} \boldsymbol{y}, \tag{5.5}$$

where $W^{[k]} = \Sigma_{\theta^{[k]}} \bar{L}^\top \left(\bar{L} \Sigma_{\theta^{[k]}} \bar{L}^\top + \Sigma_\epsilon \right)^{-1}$. As the priors favor small dipole strengths, the solution is biased to more superficial locations, which can be weaker while resulting in the same effect at the sensors. This is a well-known pitfall of minimum norm estimation methods, which standardization aims to counteract [38].

The standardization method here is the sLORETA technique [48]. For this the so-called resolution matrix is calculated as the product of the inverse and the forward operator:

$$R = W \bar{L}. \tag{5.6}$$

R can be seen as the transfer matrix between the real and estimated current densities, assuming the real data is simulated using L. In an ideal case this would be the identity matrix, but due to the non-uniqueness of the problem, the inverse operator is biased. The diagonal elements represent the distortion of the reconstruction for a unit source j (below the vector of source strengths $\boldsymbol{D}$ consists of just ones):

$$R_{jj} = \sum_{i=1}^{N} (W^{[k]})_{ji} \cdot \bar{L}_{ij} = (W\bar{L}\boldsymbol{D})_j. \tag{5.7}$$

By normalizing the reconstruction by this vector we are effectively gauging how much evidence for source activity at a particular position can be found in the data, correcting the depth bias:

$$D_j^{[k,\text{stand.}]} = \frac{D_j^{[k]}}{\sqrt{R_{jj}}}. \tag{5.8}$$

5.5.2 Gaussian Mixture Model

In order to estimate the spread of the source obtained using IAS, a Gaussian Mixture Model (GMM) was fitted to the reconstructed current density distribution. This is a clustering method also provided in Zeffiro Interface. The GMM identifies the primary concentration areas of the current density as a superposition of Gaussian distributions [24]. Since in the case of the simulated and real data the current density distribution should be unimodal, it was assumed that it is adequately represented by a single cluster. This cluster takes the form of an ellipsoid, as shown in Fig. 5.13. There are several ways to use the properties of this ellipsoid to quantify the spread of the reconstruction, e.g., via its volume. To assess whether the distribution is spread in the same direction as the synthetic source, one can measure the sectional area of the ellipsoid with the tangential and radial planes as sketched in Fig. 5.14.

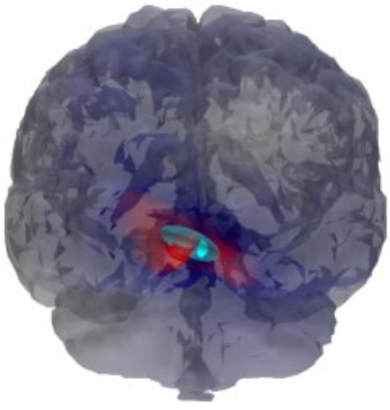

Figure 5.13: Gaussian cluster fitted to the current distribution.

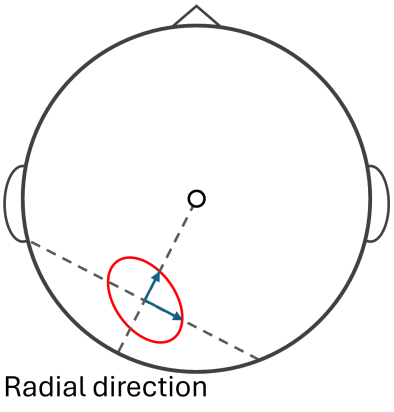

Figure 5.14: Measuring the stretch of the ellipsoid in radial and tangential direction.

6 Simulation Results

6.1 Topography Error and Single Dipole Scan

Figure 6.1 shows an example of EEG topographies resulting from a patch, in comparison to that of a single dipole at the same position as the patch center, as well as a single dipole 3 mm deeper. The topography of the deeper dipole looks almost identical to that of the patch. This is a first visualization of the depth bias caused by the extended source, where an increasing radius of the patch will lead to the dipole being mislocalized at a deeper location.

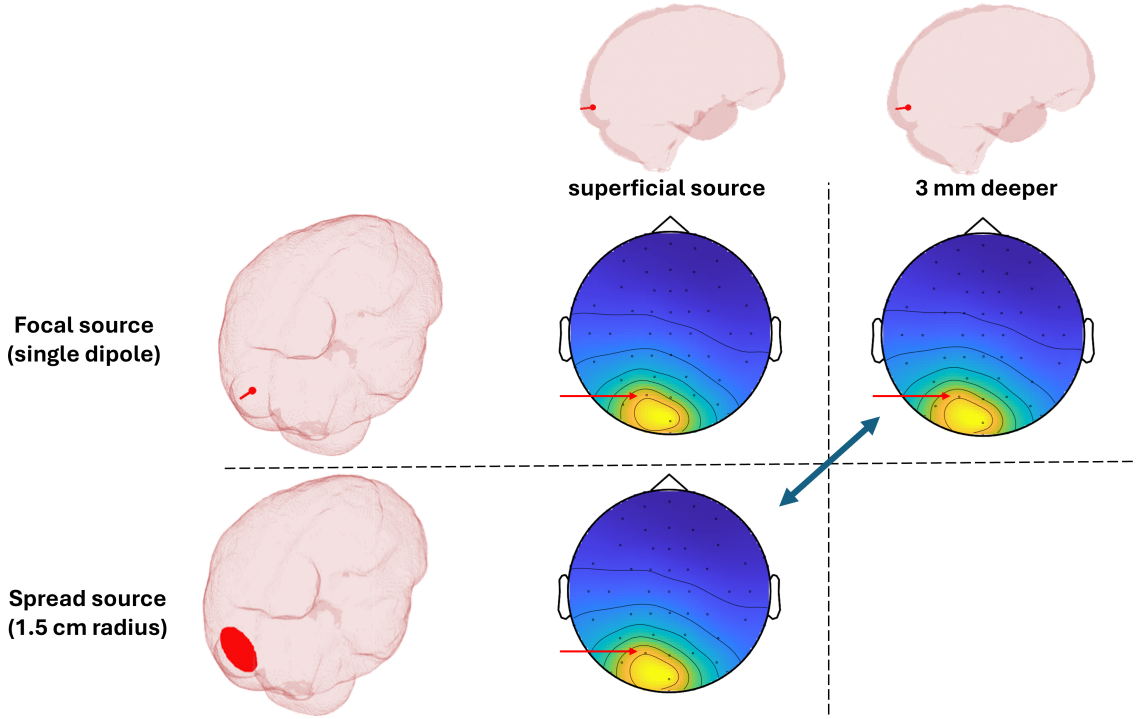

Figure 6.1: Comparison of simulated topographies for a patch and a single dipole. The difference is visible at the isopotential line near the electrode marked by the red arrow.

The similarity between two topographies/data vectors $\boldsymbol{y}_1$ and $\boldsymbol{y}_2$ can be assessed using the relative distance measure (RDM):

$$\mathrm{RDM}(\boldsymbol{y}_1, \boldsymbol{y}_2) = \frac{1}{2} \left\| \frac{\boldsymbol{y}_1}{\|\boldsymbol{y}_1\|_2} - \frac{\boldsymbol{y}_2}{\|\boldsymbol{y}_2\|_2} \right\|_2, \tag{6.1}$$

where RDM is the topography error and $1 - \mathrm{RDM}$ is the accuracy or similarity.

Figures 6.2a to 6.2c show this quantity for a patch with 15 mm radius compared with a single dipole at different positions. The tangential position of the dipole always coincides with the center of the patch, but the radial position (depth) varies. This was done for three different kinds of patches: The flat patches, as employed by de Munck (Fig. 6.2a), show a peak of the similarity just (less than 1 mm) deeper than the actual position. This means the EEG sensor measurement from a single dipole is almost identical to that of a patch. Changing the position of the dipole in any direction decreases the similarities of the topographies. While in the first patch type, all dipoles have the same moment, in the second patch type (Fig. 6.2b), they are still organized in the completely flat patch, but are oriented radially. This leads to a larger shift of the peak to a deeper location. Now, if the patch is slightly curved as introduced in Section 5.3 and the dipoles are radially oriented (Fig. 6.2c), that leads to an even larger depth shift. The EEG topography of an extended source of this type is therefore better reproduced by a dipole about 2 mm deeper, than by a dipole at the same position as the patch.

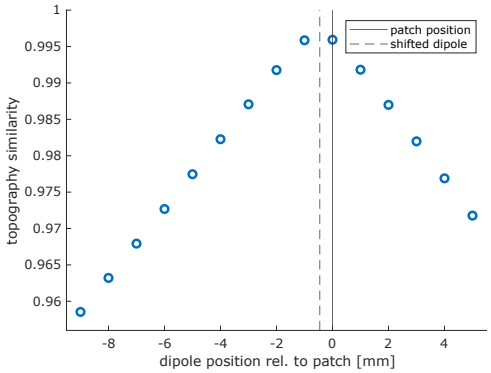

(a) Planar disk with perpendicular dipoles.

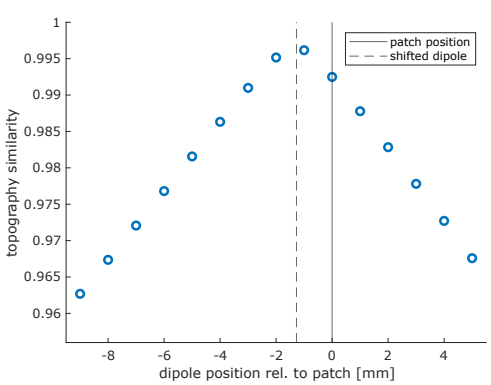

(b) Planar disk with radial dipoles.

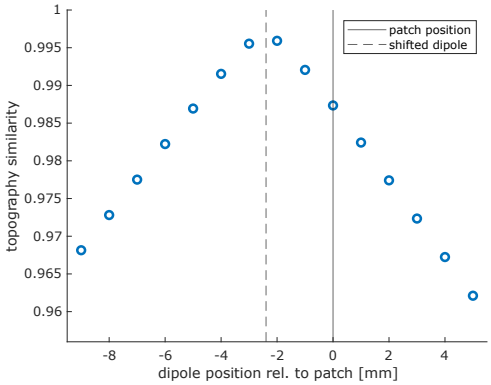

(c) Curved patch with radial dipoles.

Figure 6.2: Similarity between the EEG topography originating from a 15 mm radius patch and that of a single dipole at varying depths in the spherical head model.

By varying the radius and position of the (curved) patches, and estimating the dipole position of greatest topography similarity, we obtain Fig. 6.3. Figure 6.3a shows the result for the sphere model. Evidently, patch radii up to about 5 mm do not cause a measurable effect, but the dipole shifts deeper (up to 3 mm) relative to the patch position with increasing radius. Placing the patch deeper in the brain slightly increases the shift. The results for the FEM model (Fig. 6.3b) are of the same scale, but the effect of patch position is less consistent. For more superficial positions, the FEM model seems more sensitive to patch radius than the sphere model, for deeper positions it is the other way around. Some data is unavailable (white in Fig. 6.3b), as for the most superficial positions and large radii the patches would protrude from the realistically shaped brain.

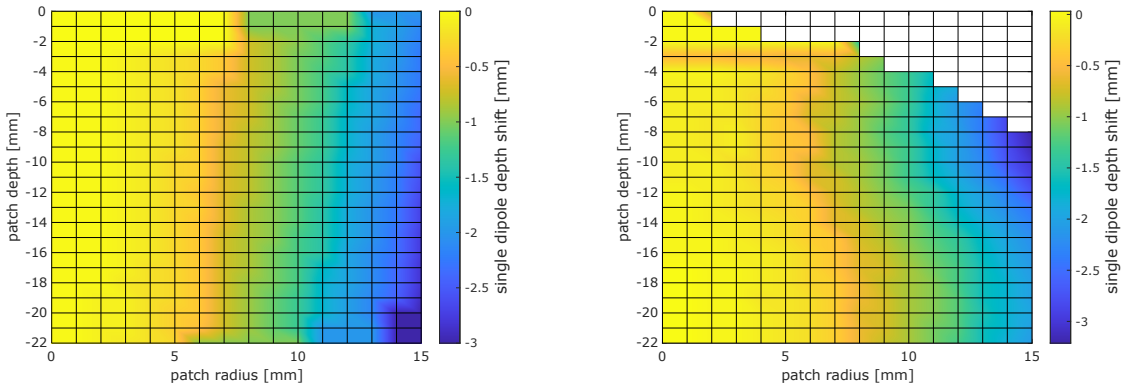

(a) Sphere model

(b) FEM with homogenized brain.

Figure 6.3: Relative dipole position with greatest topography similarity to a patch with specified radius and depth (measured from brain surface).

Applying the single dipole scan to the data confirms the result obtained using the RDM. The GOF maximized in the dipole scan is a similar measure as the RDM, except taking not only topographic distribution but also magnitude into account. Figure 6.4 shows how the GOF for a dipole at the center of the simulated patch decays as the patch radius increases, and is at some point surpassed by the GOF of deeper lying dipoles. The consequence of this is displayed in Fig. 6.5: The reconstructed dipole shifts deeper in a staircase-like fashion due to the 1 mm resolution of the source space. Due to the symmetry of the patches, the tangential position error remains zero. The dipole scan yields at each position the dipole moment that best fits the data. Figure 6.6 shows the reconstructed amplitude $\|\boldsymbol{d}_{j,\mathrm{rec}}\|_2$ normalized by the amplitude of the patch (i.e. amplitudes of all dipoles within the patch added up). The result of the dipole scan is here visualized by the dashed line. The other lines show the reconstructed amplitude for dipoles at fixed positions. As the dipole scan jumps to a different position, there is also a jump in the amplitude. There are two counteracting effects here: In general, deeper dipoles are reconstructed with a larger amplitude than more superficial ones. One might therefore expect the amplitude obtained by the dipole scan to increase with increasing patch radius, as we shift to deeper positions. However, fixing the dipole position while increasing the patch radius leads to a decrease in amplitude. This is due to the dipoles being oriented radially, which means that at the outer borders of the patch they point in increasingly different

directions and therefore partially cancel each other out. This effect is stronger than the depth shift effect, so that at the first 1 mm jump, the amplitude error is actually zero. For a radius of 15 mm, the reconstructed amplitude becomes about 2 % too small.

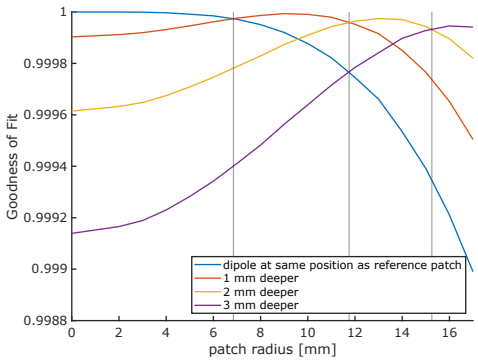

Figure 6.4: GOF for four different dipoles at fixed positions as the patch radius increases. Vertical lines mark the radii for which the GOF of a deeper lying dipole surpasses that of the more superficial one.

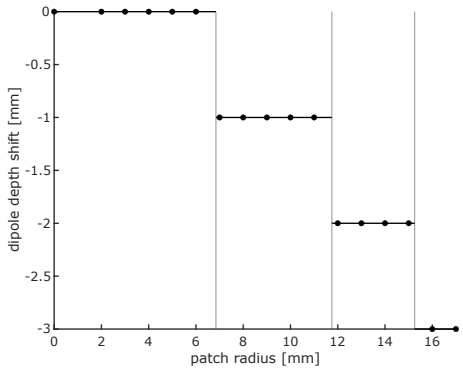

Figure 6.5: Position relative to the patch center of the dipole with highest GOF.

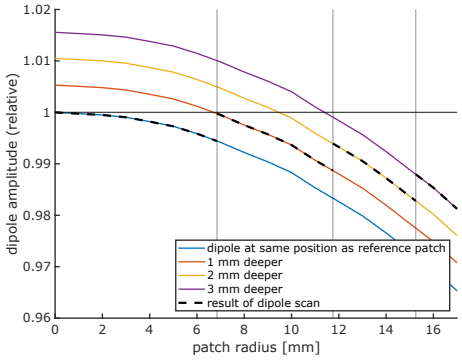

Figure 6.6: Reconstructed dipole strength divided by the total amplitude of the reference patch.

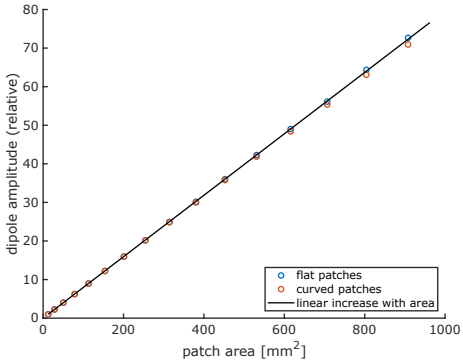

Figure 6.7: Reconstructed dipole strength relative to strength of the smallest patch.

In practical applications, it has been suggested that the size of an activated cortical patch can be estimated by the amplitude of the reconstructed dipole, with a moment of 10 nAm corresponding to 40 mm^2 [45]. However, an amplitude error caused by the source extent would skew this estimation. Figure 6.7 shows that the actual dipole amplitude (normalized by the smallest possible patch amplitude) indeed increases almost linearly with the patch area. Due to the source space resolution, the minimum area of a patch containing more than one dipole is 12.6 mm^2. Only at around 6 cm^2, which is almost 50 times that minimum area, we start to see a very small deviation from the linearity. Notably, de Munck's flat patches, where there are no canceling effects, cause here a slightly higher amplitude than the linear estimate, and the curved patches a slightly lower.

Real data is contaminated by noise, which itself causes reconstruction errors. Figure 6.8 shows that for very low noise (3 % of the maximum signal amplitude) the median of the dipole depth, calculated from 50 samples, decreases visibly with radius. For experimental data with high quality, 20 dB SNR can be reached. Here, the noise causes a much greater variance of the position. In contrast to the effects of patch size, the noise can also cause tangential mislocalization. The total position error lies around 2 mm for 30 dB and 5.5 mm for 20 dB. For 30 dB SNR, increasing the radius causes a slight increase of the total error from 2 mm to 3 mm. However, as for 20 dB, the position error caused by the noise is already larger than 3 mm, the error caused by the noise obscures that by the patch size.

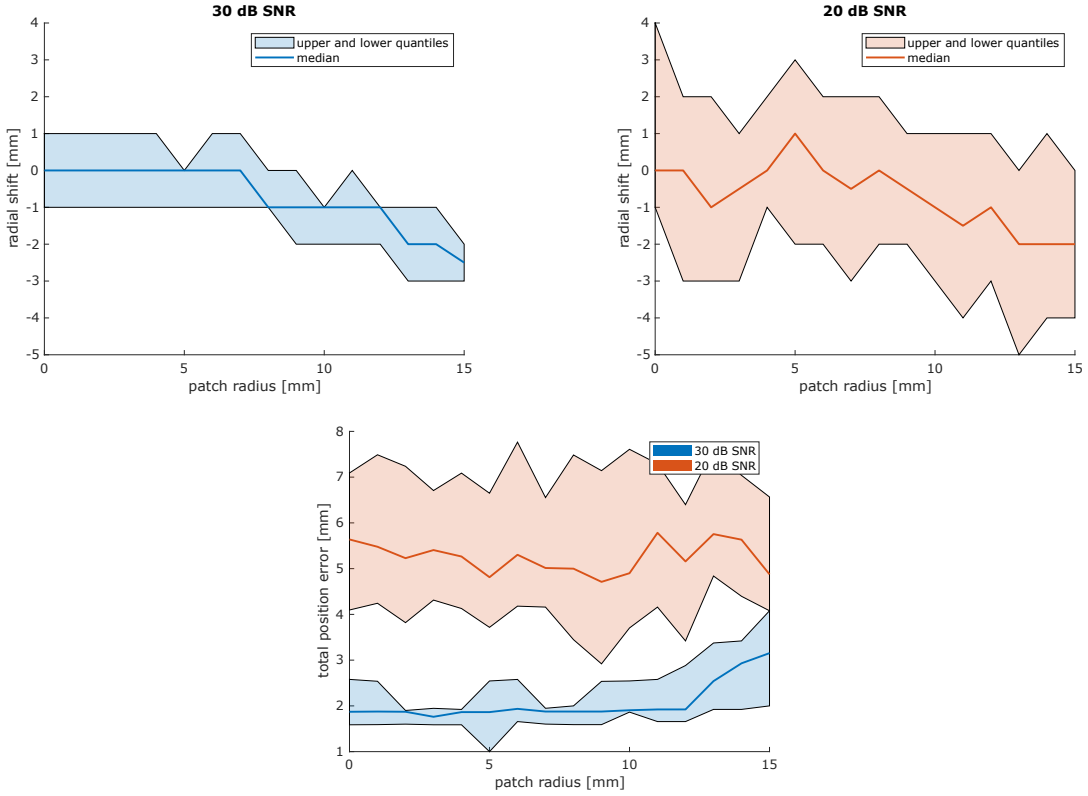

Figure 6.8: Dipole shift in radial direction (top) for 30 dB and 20 dB SNR, and total position error (bottom).

6.2 Patchy Dipole Scan Performance

Figure 6.9 shows the position error for the patchy dipole scan while varying both the reference patch radius and the radius of the patches assumed by the scan. Along the diagonal, where both radii match, the patchy dipole scan achieves zero localization error. However, if the radii do not match, the obtained errors quickly become larger than for a normal single dipole scan (equivalent to the bottom row of Fig. 6.9). This now also includes tangential errors, whereas the single dipole scan only exhibited a radial shift.

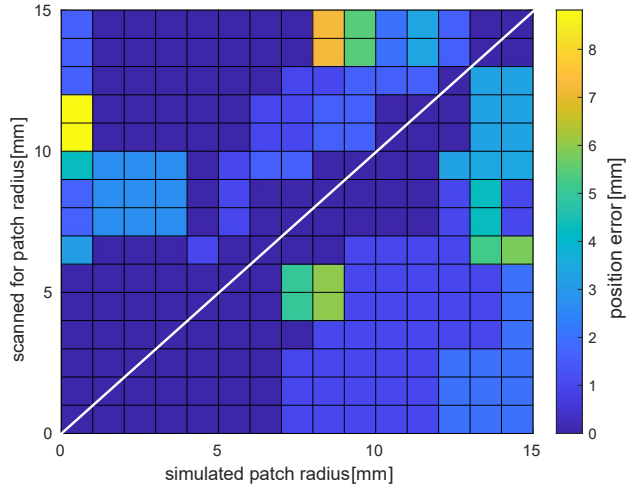

Figure 6.9: Localization error of the patchy dipole scan with varying simulated source radius and radius assumed by the scan.

Another property of the patchy dipole scan is that it is more computationally expensive than the single dipole scan. This is due to the calculation of the pseudoinverse, which needs to be done for each position in the source space, taking longer for larger leadfield subsets, i.e., for more dipoles per patch. The pseudoinverse is calculated using the Matlab function *pinv*, whose computational complexity is not documented. But as shown in Fig. 6.10, the patchy dipole scan with 10 dipoles per patch takes about 10 times longer than a single dipole scan, using Matlab 2022b on a system with Intel Core i7-6700 and 32 GiB RAM, running Ubuntu 22.04.

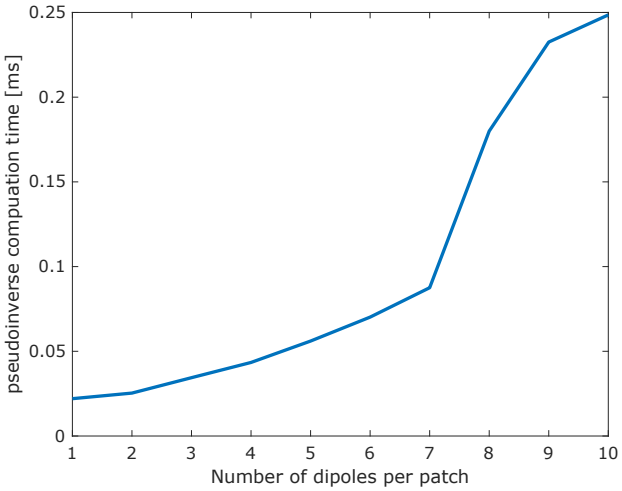

Figure 6.10: Time to calculate pseudoinverse for a subset of the leadfield matrix pertaining to the specified number of dipoles.

6.3 IAS for Simple and Complex Extended Sources

The following graphs show the effect of varying tail length on several properties of the reconstructed current density. Simulated sources with four different extents were used: single dipole, and patches with radius 5, 10 and 15 mm. Visualized are the median values and interquartile ranges of the respective parameters, obtained from 20 samples.

1) Low noise, radial dipoles

In the case of the flat patches with radial dipoles in the FEM model with homogenized brain and low noise, small but consistent differences between the different sources can be seen, and increasing the tail length leads to smooth curves.

Figure 6.11 shows the l_1-norm computed over the whole reconstruction. A small l_1-norm is an indicator of fewer active sources. The l_1-norm decreases as the hyperprior tail length increases. The reconstruction for the largest of the simulated patches consistently maintains a higher median l_1-norm and ranges to higher values than for the single dipole. The two medium sized patches lie within the interquartile ranges of the single dipole and the largest patch, and thus can not be distinguished here.

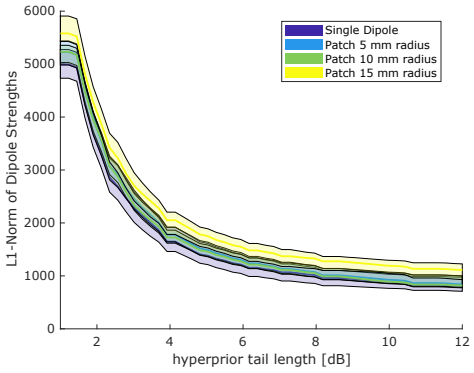

Figure 6.11: l_1-Norm of the reconstruction for patches with radial dipoles (30 dB SNR, EEG).

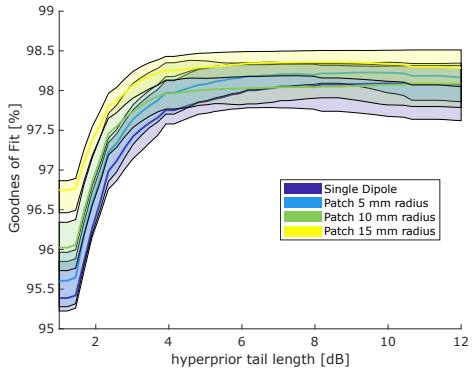

Figure 6.12: GOF of the reconstruction for patches with radial dipoles (30 dB SNR, EEG).

The GOF (Fig. 6.12) increases by about 2 % (96.7 to 98.3 % for the 15 mm patch) with increasing tail length up to about 4dB. For tail length <4 dB, the single dipole has about 1 % lower GOF (95.4 % at 1 dB) than the largest patch but for >4 dB, the GOF for the single dipole continues rising (up to 98.0 %) while it remains relatively constant for the 15 mm patch.

A more intuitive measure for the extent of the source distribution than the l_1-norm is obtained from the Gaussian cluster fitted to the reconstruction. The projected radius (Fig. 6.13) is calculated from the sectional area of the ellipsoid and the tangential plane by $r_{\text{proj}} = \sqrt{\frac{A_{\text{sect}}}{\pi}}$, thus expressing the spread of the distribution in tangential direction, i.e., the direction in which the reference source is also spread. We can divide this by the total volume of the ellipsoid, or rather the equivalent radius $r_{\text{equ}} = \left(\frac{3V_{\text{elip}}}{4\pi}\right)^{\frac{1}{3}}$, to get a relative measure for how much the ellipsoid is stretched from a sphere in tangential direction (Fig. 6.14), where a value of 1 would indicate a spherical distribution. As indicated by the l_1-norm, the projected radius decreases with increasing tail length, though the curves are less smooth. For larger tail lengths, the median radii of the four different sources converge (ranging from 4.6 to 6.4 mm for 1 dB, and 3.2 to 3.5 mm for 12 dB). However, the tangential stretch remains relatively constant for the single dipole (1.07) while it increases from 1.08 to 1.15 for the 15 mm patch. This means that for small tail lengths, the distribution is spread in both radial and tangential direction, while for larger tail length, although the absolute radius decreases, the ellipsoid becomes more stretched in tangential direction. For the single dipole on the other hand, the relative shape of the ellipsoid is less affected by the tail length.

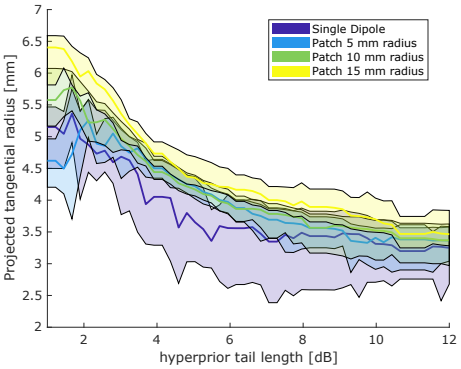

Figure 6.13: Projected radius in tangential direction (30 dB SNR, radial dipoles, EEG).

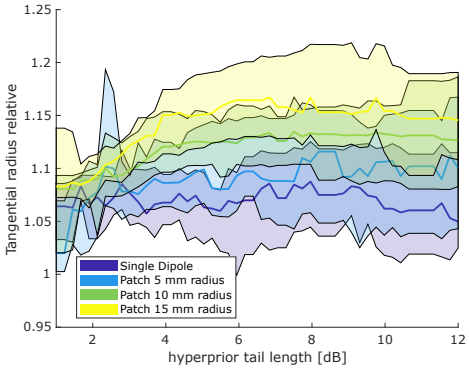

Figure 6.14: Relative stretch in tangential direction (30 dB SNR, radial dipoles, EEG).

To assess localization accuracy, the distance between the center of the ellipsoid is compared to the center of the reference patch (Fig. 6.15). For the 15 mm patch this is lowest for small tail lengths and increases from 1.8 mm to 5.1 mm. The single dipole and the 5 mm patch show some instability up to about 4 dB. Then, the single dipole remains at a constant error of 3.7 mm, while the error for the 5 mm and also the 10 mm increases as it does for the 15 mm patch. Regarding the depth error (Fig. 6.16), which is the distance in radial direction, the instability for below 4 dB is also visible. In the stable region, the larger the patch, the deeper it is reconstructed, though the error in radial direction remains under 2 mm even for the 15 mm patch, increasing slightly by 0.5 mm with increasing tail length.

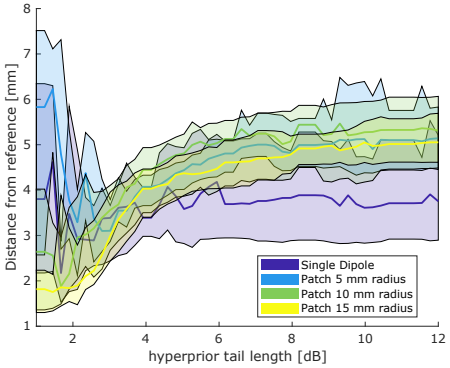

Figure 6.15: Distance of reconstruction ellipsoid center from reference patch center (30 dB SNR, radial dipoles, EEG).

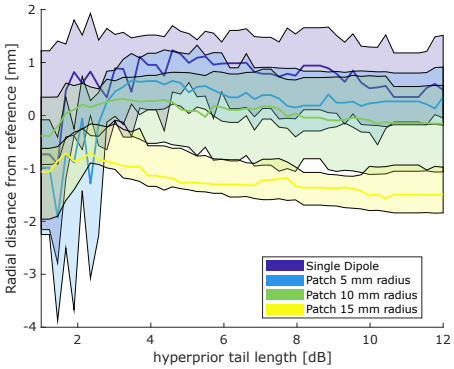

Figure 6.16: Depth shift of reconstruction ellipsoid center from reference patch center (30 dB SNR, radial dipoles, EEG).

2) Low noise, cortex-normal dipoles

In the 6-compartment FEM model, dipoles are positioned in the gray matter only, and their orientation in the patches is normal to the cortex surface. This drastically changes the results for patches at the same position compared to the homogeneous and symmetrical patches with radially oriented dipoles.

There remains an overall trend of the radius decreasing with increasing tail length, however, the actual reference source radius seems to have unpredictable effects (Fig. 6.17). For a 12 dB tail length, the reconstructed extent of the 15 mm patch is actually **below** that of the single dipole (3.6 mm to 4.0 mm). The localization error (Fig. 6.18) is also inconsistent, and in parts the highest for the single dipole. For small tail lengths the error is over 10 mm and then decreases for all reference sources to around 4.7 mm, which is also larger than for the radially oriented single dipole.

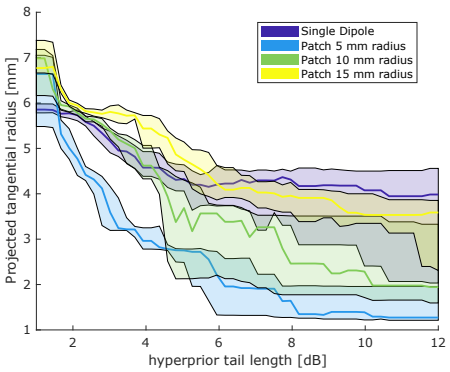

Figure 6.17: Projected radius in tangential direction (30 dB SNR, cortex-normal dipoles, EEG).

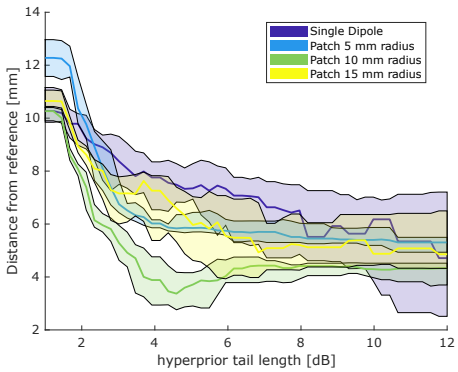

Figure 6.18: Distance of reconstruction ellipsoid center from reference patch center (30 dB SNR, cortex-normal dipoles, EEG).

We can now also evaluate the MEG, which was previously not discussed due to its insensitivity to radial sources. Here, the reconstruction results are more consistent with the radii of the reference sources. The l_1-norm (Fig. 6.19) for the 15 mm patch is consistently larger than the norm for the single dipole with no overlap of the interquartile ranges. However, for the 5 and 10 mm patches the medians are very similar and ranges strongly overlap. Up to a tail length of 4 dB, the equivalent radius (Fig. 6.20) correctly increases with increasing reference patch radius (7.5, 7.6, 7.8 and 8.0 mm for the four different sources at 1 dB). At >4 dB the order of curves is inconsistent with the true radius.

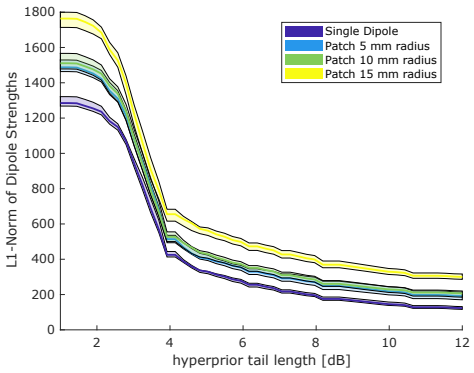

Figure 6.19: l_1-Norm (30 dB SNR, cortex-normal dipoles, MEG).

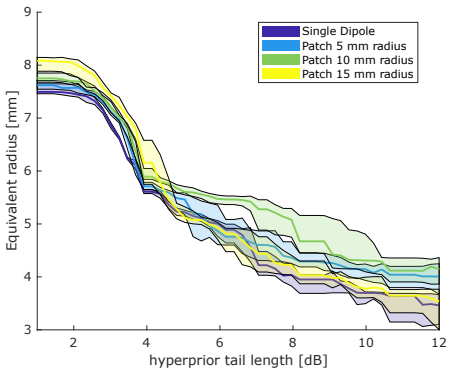

Figure 6.20: Equivalent radius (30 dB SNR, cortex-normal dipoles, MEG).

While the extent is better represented for tail lengths <4 dB, in this region, the localization error is much larger (15.7 mm for the 15 mm patch) than in the region >4 dB (Fig. 6.21). At 4 dB, the localization error is about the same (4.5 mm) for all patch sizes, and decreases for the single dipole to 2.6 mm while increasing for the 15 mm patch to 4.9 mm with increasing tail length. Figure 6.22 shows that the 15 mm patch is reconstructed up to 7 mm deeper than the single dipole.

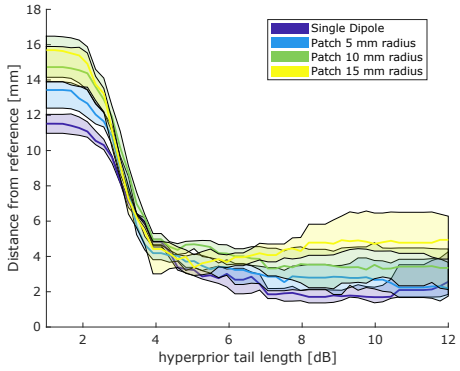

Figure 6.21: Distance (30 dB SNR, cortex-normal dipoles, MEG).

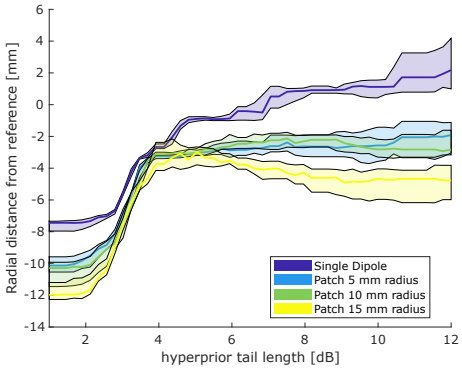

Figure 6.22: Depth shift (30 dB SNR, cortex-normal dipoles, MEG).

3) High noise, radial dipoles

For a lower SNR of 20 dB, the global trends visible at 30 dB remain, but distinction between patches of different radii becomes difficult. Two regions, <4 dB and >4 dB tail length can again be identified. First, the radius (Fig. 6.23) increases (4.1 mm to 5.2 mm for the 15 mm patch). Then, for >4 dB, it decreases to 4.4 mm. That is larger than the 3.5 mm obtained at 30 dB SNR. For the single dipole, in comparison to 30 dB SNR, the noise intervals are larger but the median radius is not (median 3.1 mm with IQR 2.9-4.5 mm for 20 dB, median 3.2 mm with IQR 2.7-3.6 mm for 30 dB). In regards to the distance of the reconstruction from the reference source (Fig. 6.24) it seems to be generally beneficial to have a tail length of about 6 dB, as this decreases the localization error for all reference sources from over 15 mm to about 6.5 mm.

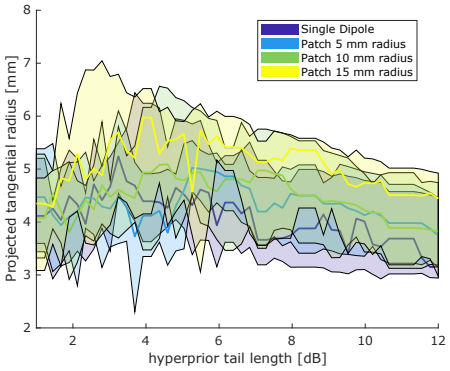

Figure 6.23: Projected radius (20 dB SNR, radial dipoles, EEG).

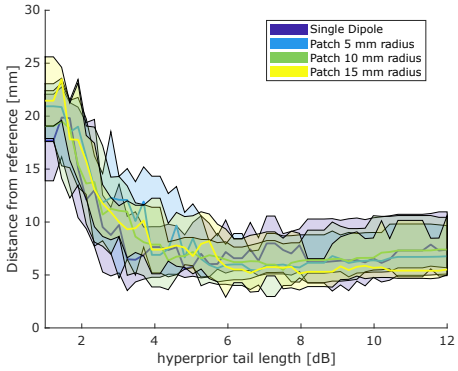

Figure 6.24: Distance (20 dB SNR, radial dipoles, EEG).

4) High noise, cortex-normal dipoles

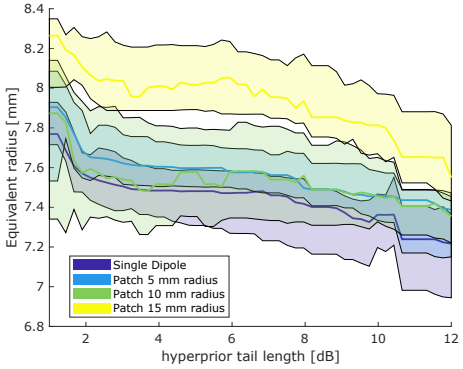

Figure 6.25: Radius (20 dB SNR, cortex-normal dipoles, MEG).

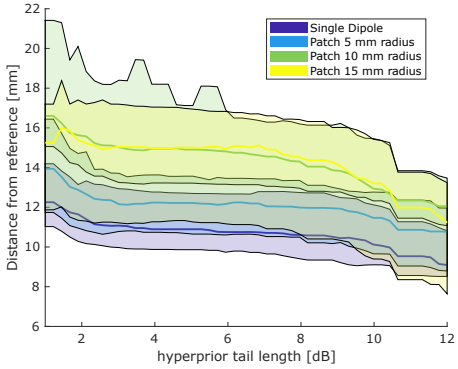

Figure 6.26: Distance (20 dB SNR, cortex-normal dipoles, MEG).

For the patches with cortex-normal dipoles at 20 dB, the EEG case is as unpredictable as for higher SNR. In the MEG case, results are again more consistent. Both the radius (Fig. 6.25) and the localization error (Fig. 6.26) decrease with the tail length, but the strong drop at <4 dB exhibited at 30 dB SNR does not occur here: The radius for the single dipole falls from 7.8 to 7.2 mm, still about double the radius at 30 dB SNR. The distance falls from 12.3 to 9.1 mm. As in previous results, the 15 mm patch can be clearly distinguished from the single dipole by its size and distance (7.6 mm radius, 11.2 mm distance at 12 dB). The 5 mm and 10 mm patches on the other hand exhibit in parts the same median radius, and the 10 mm patch in parts the same median distance as the 15 mm patch.

6.4 Discussion of Simulation Results

For flat, tangentially extended source patches, the simulations have shown a small, but systematic localization error of the single dipole scan: Dipoles are reconstructed up to 3 mm too deep for a synthetic source patch with 15 mm radius. Extents above that are physiologically unlikely in this context, as discussed in Section 2.2. These values coincide with de Munck's results, who reported a depth error of 2 % for a patch radius of 15 % of the head radius. For the head model used in this thesis, which has a head radius of 94 mm, this corresponds to a patch radius of 14.1 mm and a depth shift of 1.9 mm [43]. Errors of this magnitude are negligible in real experimental data compared to other error sources, especially measurement noise, but also factors like modeling inaccuracies and subject movement. In a detailed FEM model where dipoles are constrained to the cortical surface, the depth bias may not manifest at all if there is simply no dipole in the source space at a position just a few mm deeper. Furthermore, realistic source patches following the cortical surface can also extend radially along a sulcal wall, which de Munck has shown actually causes a bias towards more superficial positions.

Nevertheless, it was also shown that, with dipoles oriented perpendicular to the patch surface, a curvature of the patch leads to an increased localization error compared to planar patches. This can be explained in the case of quasi-radial dipoles by an increased area of effect at the scalp. At the same time, canceling effects lead to an amplitude error which counteracts and eventually surpasses the amplitude error caused by the depth bias. This suggests that increasing the curvature or inverting it, which could be used to model an extended source along a gyrus crown or sulcal valley, may lead to more significant errors. In that case, the amplitude of the reconstructed dipole may not be a reliable way to estimate the extent of the true source. However, for the patches as implemented in this thesis, the popular assumption that an extended source can be accurately reconstructed by a single dipole, and that the extent can then be inferred from the dipole strength, is valid.

As for the patchy dipole scan, this method is able to achieve zero error where the dipole scan gains a bias due to source extent. However, the radius needs to be exactly known beforehand, as deviations of 1 mm can already lead to errors larger than in the

single dipole scan. If the source actually is a single dipole, misapplying the patchy dipole scan and assuming a large extent can lead to errors up to 8 mm. Therefore, in this scenario, the single dipole scan provides a more robust reconstruction method. One can imagine though, that in more complex scenarios where patches follow the local cortex structure, the patchy dipole scan might outperform the single dipole scan in a meaningful way. The difficulty of this method is that it always enforces a rigid constraint on the geometry of allowed source patches. Even if the patches are implemented to follow the cortical surface, the expected size needs to be set a-priori.

In contrast, the advantage of the IAS algorithm is that the constraints on the solution are not rigid. This makes it capable of reconstructing multiple sources (though not investigated here) and extended sources without the user having to explicitly fix a certain number or size. Because the priors are updated empirically, even if the algorithm is biased towards focal reconstructions by a high tail length, the extent of the reconstruction still reflects the extent of the underlying reference source. Nevertheless, at least in the case of low noise and radial dipoles, enforcing focality leads to an increased localization error for the patches, while not affecting the single dipole. The differences between reconstructions for sources with varying extents amount to a few mm though, just as in the dipole scan, and the true extents can not be reproduced. Additionally, the extent of the reconstruction seems to, at least partially, correspond to a region of uncertainty, which increases with increasing noise. This may become a problem for experimental data, where smaller patches also exhibit lower SNR.

Changing from radial dipoles to cortex-normal dipoles drastically changes the EEG reconstruction results. The location of the single dipole, which coincides with the center of the patches, was chosen so that the combined net orientation of the dipoles within a patch should not differ too much from the orientation of the single dipole. However, differences can not be avoided: For the 5 mm radius patch the difference in net orientation is 16°, for 10 mm it is 49° and for the 15 mm it is 68°. Additionally, the dipoles are also unsymmetrically distributed across a patch, as they can only be in the gray matter. These two factors presumably led to unpredictable effects when increasing the patch size. Evidently, there are steps missing between the simple and complex patch types, that could help understanding the results. Quantifying the net dipole moment and the real center of mass of the patches and analyzing their effects on the IAS algorithm may improve the understanding of its performance in such cases. In the end, these results show that one should be wary in applying conclusions from overly simplified simulations to realistic data.

In many of the results, for radial as well as cortex-normal dipoles, a clear distinction could be made between the regions below and above 4 dB tail length. There is a steep decay in extent and position error <4 dB followed by a region of relatively little change. Increasing the tail length much higher than that is unmotivated, as it may lead to slightly more focal results, but does not improve localization or GOF. Therefore, for the evaluation of the experimental data, the tail length will be set at 6 dB.

7 Experimental Results

7.1 Sensor-Level Analysis

In the first step, the measurement data from different participants and stimuli is evaluated on a sensor-level, and adequate data is selected, before proceeding with the inverse analysis. Figure 7.1 exemplifies how strongly results from different subjects and measurement runs can differ, justifying a preliminary quality check. The figure shows the signal time-course at all sensors, visualized as a butterfly plot for two different measurement runs. While the left plot represents a low noise measurement with a very clear N75, resulting from Subject 8, stimulus Third 2, the right plot shows a measurement where no signal is visible above the noise, i.e., a SNR of 0 dB, resulting from Subject 6, stimulus Third 3.

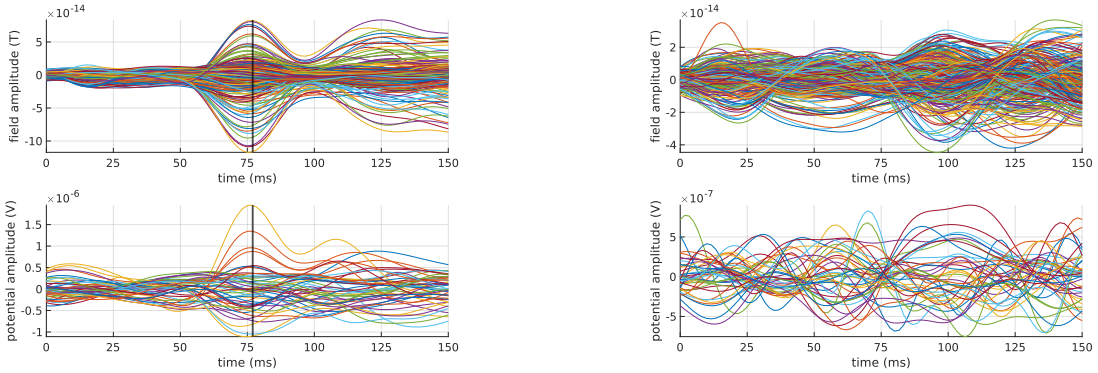

(a) Subject 8, stimulus Third 2

(b) Subject 6, stimulus Third 3

Figure 7.1: Butterfly plots (signal at all sensors) of the measured VER MEG field amplitude MEG (top) and EEG potential amplitude (bottom).

Figure 7.2 shows the topographical distribution of the MEG field amplitude and EEG potential amplitude during the N75 peak, for Subject 8 and all stimuli. From the differences in topography one can conclude that the underlying source orientation rotates for the different stimuli. Notably, for Third 3 the EEG changes dramatically while the MEG remains similar to Third 2, suggesting a dominant radial component.

Due to the low signal strength in the MEG for the Third 3 stimulus (note that the signal range is about half that of the full stimulus) an artifact that appears to be an activation in the frontal sensors becomes visible. This is caused by a magnetic screw attaching the stimulus presentation screen to the MEG, that was found only after the measurements of all subjects had concluded. This does not negatively affect inverse results, as frontal magnetometers (42 of 272) were consequently excluded from the data for analysis. Further justification for this is the activation from the visual stimuli being firmly contained to the back of the head where the visual cortex is located. Therefore, frontal MEG sensors contain only noise and would lower SNR and GOF while not contributing to source localizability.

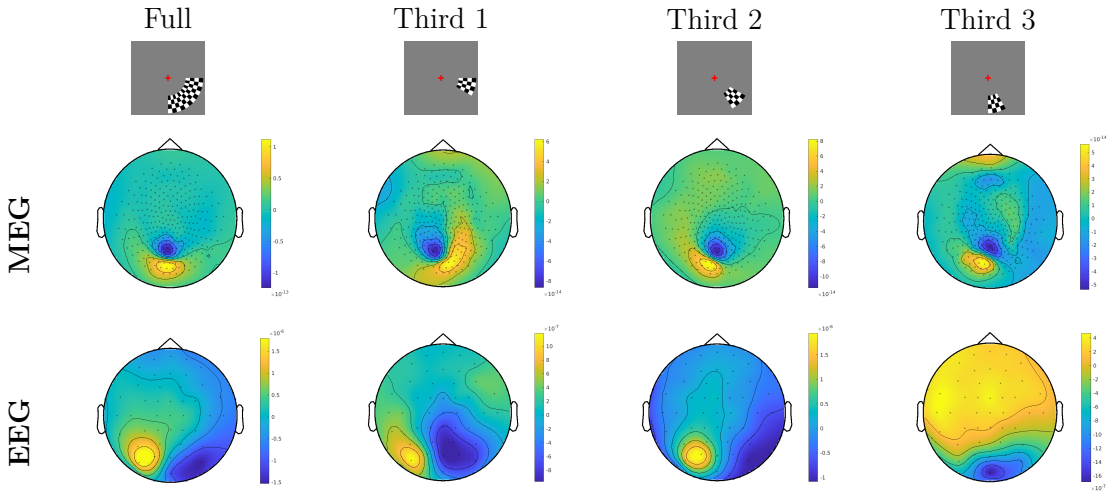

Figure 7.2: Topology (view from above on the head) of MEG and EEG measurements for Subject 8.

Table 7.1 show the signal to noise ratios for all participants and stimuli in MEG and EEG, where a SNR>10 dB is considered "good" (low level of noise).

Ideally, head movement during the measurement should be below 5 mm, but this was not achieved for all stimuli in all subjects. Marked in the table are measurement runs for which head movement above 5 mm was measured, as the SNR could be affected. While it is possible the head movement is connected to measurement duration, the order of stimulus presentation was randomized so there is no correlation between head movement and stimuli. Coincidentally, all measurement runs using the full quadrant stimulus fall below the limit of 5 mm.

Table 7.1: Signal-to-Noise-Ratio [dB] of the measurement data per subject and stimulus. *MEG and EEG data excluded. **EEG data excluded.† Head movement >5 mm.

MEG

Subject	Full	Third 1	Third 2	Third 3
1	22	18	19	11†
2	13	10	6	7
3*	6	5	3	3†
4	22	7	16	15
5	16	16†	17†	7†
6	13	7†	11†	0†
7	12	7	15	7
8	14	16	16	12

EEG

Subject	Full	Third 1	Third 2	Third 3
1	19	21	15	10
2	14	9	6	3
3*	3	10	4	2
4	19	12	17	11
5	7	6	12	6
6	7	5	8	1
7**	5	-1	-1	4
8	10	7	10	8

As marked in the table, data from two subjects will be omitted from further analysis as the observed low SNR is likely caused by external factors, and not by inherent properties of the underlying activation:

(1) Subject 3 MEG and EEG data is omitted as the N75 component could not be identified in the signal time course for any of the stimuli. This is likely due to a strong refractive error (-4.5 dpt right, -5.0 dpt left) which may have not been adequately corrected by the MEG-safe replacement glasses. Uncorrected refractive error was shown to significantly alter the pattern-reversal VER (decrease of 2.6 µV and increase of 15 ms of P100 amplitude and latency per dpt for 0.25° checks [36]).

(2) Subject 7 EEG data is omitted though the MEG data remains included. The high noise in the EEG is a result of overall poor electrode contact due to hair texture.

For all remaining participants, good SNR for the full stimulus is reached in MEG. In EEG the values are in most cases lower than in MEG, which is typical for superficial and tangential sources [49]. The relation between the SNRs of the smaller stimuli versus the large stimulus ($\frac{\sigma_{\text{Full}}}{\sigma_{\text{Third i}}}$, where σ_i is the linear relative noise) in each subject is shown in Fig. 7.3.

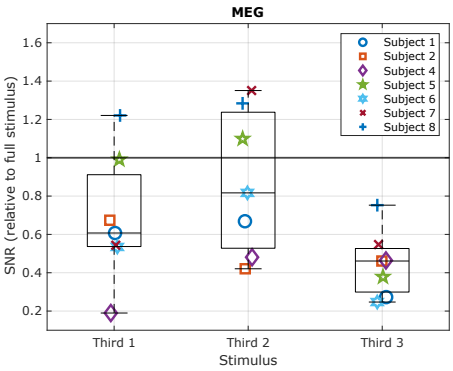

(a) Medians: Third 1: 0.61 (IQR 0.54-0.91), Third 2: 0.82 (IQR: 0.53-1.26), Third 3: 0.46 (IQR: 0.3-0.53).

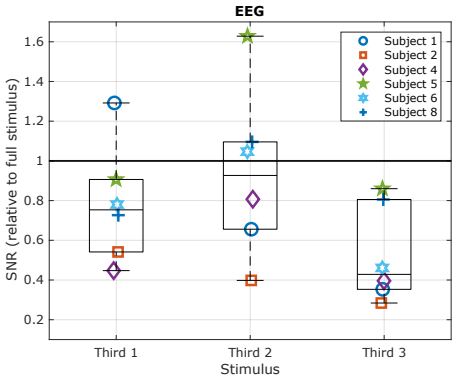

(b) Medians: Third 1: 0.75 (IQR 0.54-0.91), Third 2: 0.93 (IQR 0.66-1.10), Third 3: 0.43 (IQR 0.35-0.81).

Figure 7.3: SNR for the three small stimuli relative to the SNR for the large stimulus per subject.

The SNR tends to be lower for the small stimuli than for the full stimulus, with Third 2 having the highest median value of the three and Third 3 the lowest. For some participants, SNR is higher for Third 1/Third 2 or both than for the full stimulus, but never for Third 3.

Assuming that the activated areas for the three small stimuli can be simply added up to form one large activation area, the added up EEG/MEG signals should equal that of the full stimulus. Figure 7.4 shows the result of adding the three measurement vectors together for Subject 8.

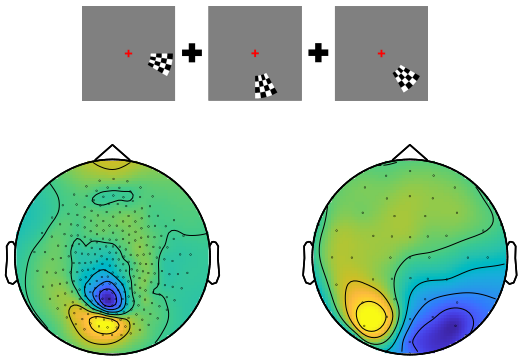

Figure 7.4: Topology (left: MEG, right: EEG) resulting from adding together the measurements for the three small stimuli (subject 8).

Visually, the topography appears similar to that of the full quadrant in Fig. 7.2. Quantitatively, this can be assessed using the RDM as in Section 6.1. Table 7.2 shows - for Subject 8 as an example - what is essentially a correlation matrix between the different stimuli, with regard to how strongly the topographies coincide. For MEG, the full quadrant and the combination of all three stimuli have the strongest match of 78 %. Third 2 lies closely behind at 72 %, while comparing, e.g., Third 1 with Third 2 only yields 36 %. For EEG, the match between the full quadrant and Third 2 is slightly higher (69 %) than between the full quadrant and the combined stimuli (67 %).

Table 7.2: Topography similarity (1-RDM) between the full stimulus, the three small stimuli, and their combined data vector for subject 8.

MEG

	Full	**Third 1**	**Third 2**	**Third 3**	**Combined**
Full	1				
Third 1	0.51	1			
Third 2	0.72	0.36	1		
Third 3	0.59	0.36	0.65	1	
Combined	0.78	0.57	0.73	0.68	1

EEG

	Full	**Third 1**	**Third 2**	**Third 3**	**Combined**
Full	1				
Third 1	0.44	1			
Third 2	0.69	0.33	1		
Third 3	0.45	0.44	0.37	1	
Combined	0.67	0.6	0.59	0.64	1

Figure 7.5 shows the same relations in median when evaluated over all participants as described for Subject 8. Third 3 differing strongly from the full stimulus, and Third 2 being the most similar, is a trend that will continue to be apparent in the inverse results as well.

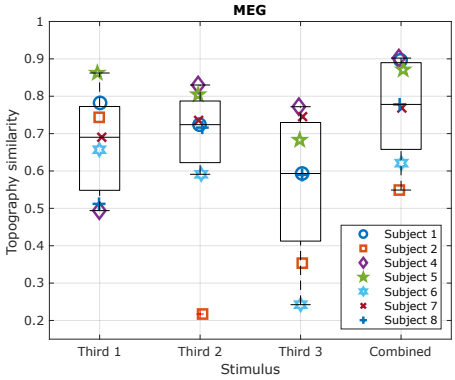

(a) Medians: Third 1: 0.69 (IQR 0.55-0.77), Third 2: 0.72 (IQR: 0.62-0.79), Third 3: 0.59 (IQR: 0.41-0.73), Combined: 0.78 (IQR: 0.66-0.89).

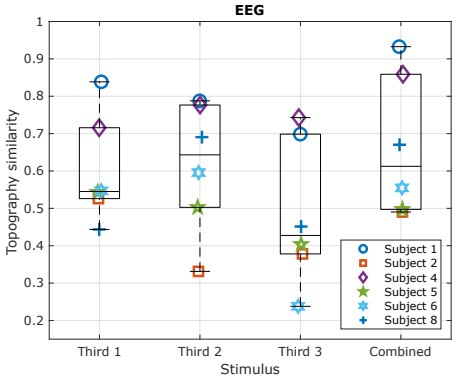

(b) Medians: Third 1: 0.55 (IQR 0.53-0.72), Third 2: 0.64 (IQR 0.50-0.78), Third 3: 0.43 (IQR 0.38-0.70), Combined: 0.61 (IQR: 0.50-0.86).

Figure 7.5: Topography similarity (1-RDM) between the full stimulus, the three small stimuli, and their combined data vector for each subject.

7.2 Statistical Analysis of Dipole Scan Results

As mentioned, the SNR for the full stimulus is good across all included participants, while some data for the small stimuli is very noisy. Furthermore, from the simulation results (Section 6.1) the localization error caused by the underestimated extent of the full stimulus is expected to be at most a few mm. Therefore, the reconstructed dipole position for the full stimulus is assumed to be a reliable initial estimate. The dipole scan for the small stimuli was then restricted to a ROI of 2 cm radius around the position found from the full stimulus, in order to ensure more accurate reconstructions even for the noisy data. Following this, results with a GOF below 70 % were deemed unreliable and excluded from further analysis, a generous selection criterion as a common threshold is 75 % [50][21].

Figure 7.6 shows the GOF of the reconstructed dipoles. For the full quadrant stimulus in MEG the GOF is firmly clustered around 91 % with a much smaller IQR (89-93 %) than any of the other stimuli. In the EEG the median is similar at 93 %, the IQR (84-97 %) larger than for the MEG, but still smaller than for the other stimuli in EEG. Across the three small stimuli, Third 2 exhibits the highest median GOF, followed by Third 1, and Third 3 the lowest. In the MEG, the median for Third 2 is 92 %, which is even higher than for the full stimulus, though values across participants go as low as 66 %. In the EEG, Third 2 has the most measurement runs across the small stimuli that pass the selection criterion of 70 %, with data from only one subject being excluded.

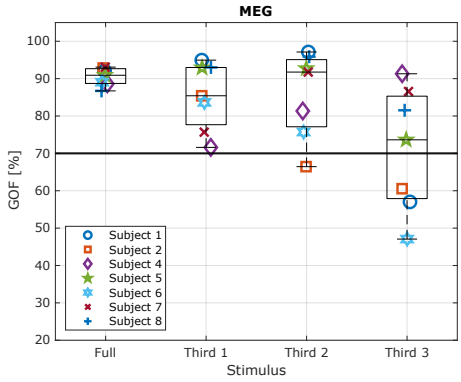

(a) Medians: Full: 91 (89-93), Third 1: 85 (78-93), Third 2: 92 (77-95), Third 3: 74 (58-85) %.

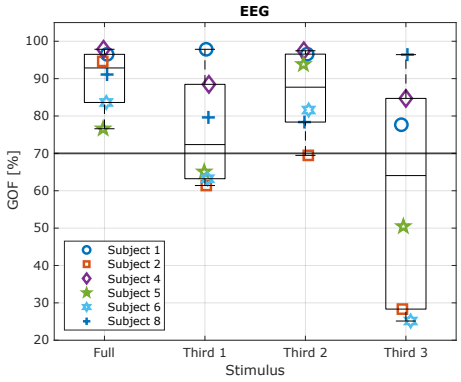

(b) Medians: Full: 93 (84-97), Third 1: 72 (63-88), Third 2: 88 (78-97), Third 3: 64 (28-85) %.

Figure 7.6: GOF of the reconstructed dipole across participants and stimuli. Horizontal line marks 70 %, below which reconstruction results are excluded from further analysis.

Figure 7.7 now shows the GOF of the small stimuli relative to that of the full stimulus per subject. In the relative visualization, it becomes evident that it is the same three subjects (1, 5 and 8) for which Third 1 and 2 reach higher GOF values than the full stimulus for MEG, and partially for EEG. Across participants, the GOF is generally lower for the small stimuli. Although, for Third 2, the difference is small, with a relative value of 0.99 in both MEG and EEG.

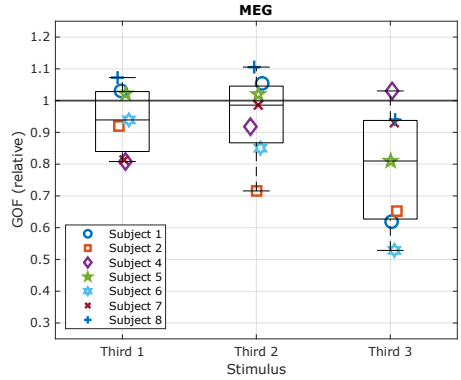

(a) Medians: Third 1: 0.94 (0.84-1.03), Third 2: 0.99 (0.87-1.05), Third 3: 0.81 (0.63-0.94).

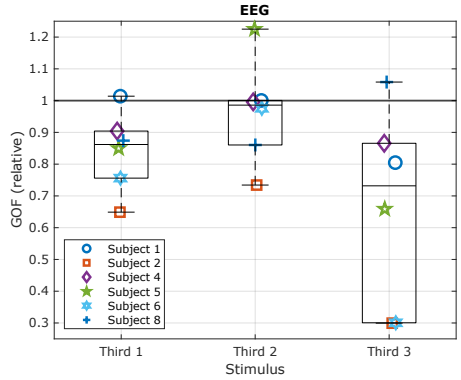

(b) Medians: Third 1: 0.86 (0.76-0.9), Third 2: 0.99 (0.86-1.00), Third 3: 0.73 (0.3-0.87).

Figure 7.7: GOF of reconstructed dipole for the small stimuli, relative to the subject-respective GOF for the full stimulus.

Having excluded questionable results on the basis of the GOF, the next step is to analyze the position and strength of the reconstructed dipoles. One way to do that in a group study is to average the functional data (i.e. the GOF at each position in source space) across subjects using the individual source spaces transformed and interpolated onto a template MRI. For details on this procedure see [51]. Figure 7.8 shows the averaged GOF on the MNI152 template brain [76], where the data colorized constitutes the top 15 % of the whole data range.

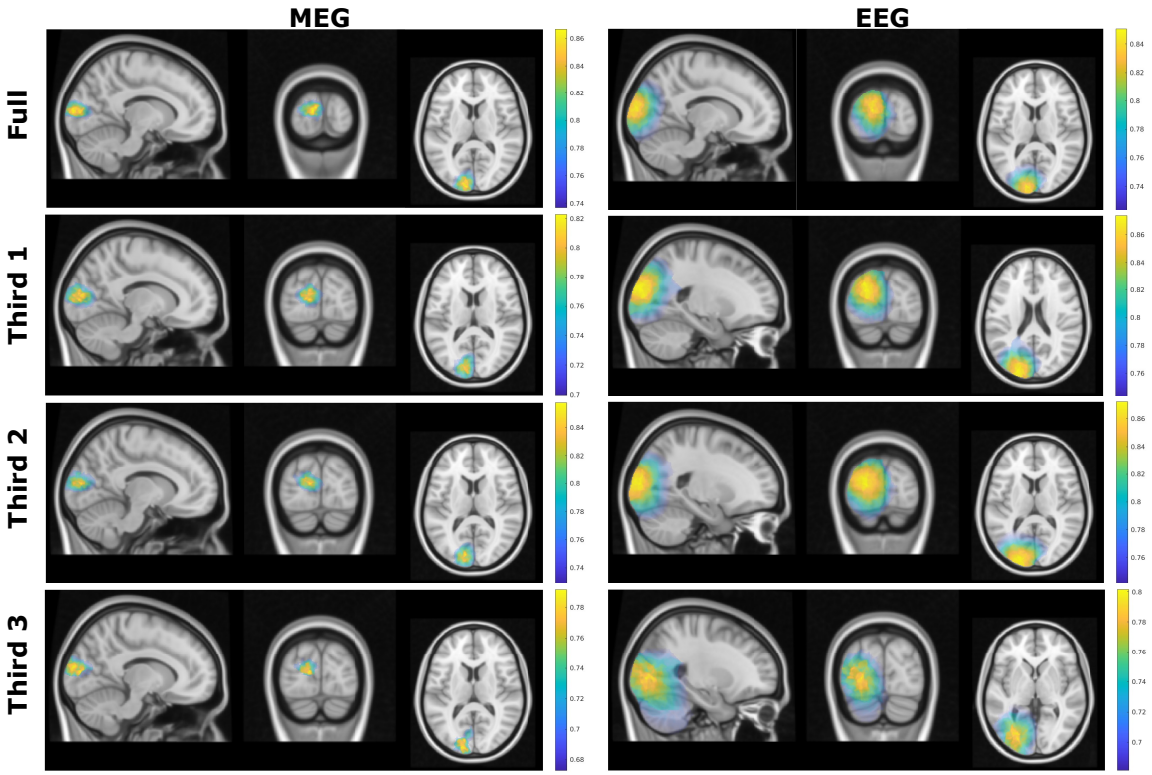

Figure 7.8: Average of GOF over subjects on MNI152 template. Shown are the top 15 % for each stimulus and modality. Due to earlier exclusion criteria the number of subjects per stimulus and modality varies (MEG: Full n=7, Third 1 n=7, Third 2 n=6, Third 3 n=4; EEG: Full n=6, Third 1 n=3, Third 2 n=5, Third 3 n=3).

The maximum of the GOF is reached as expected in the left hemisphere and approximately above the calcarine fissue. The volume in which the top 15 % of GOF lie is significantly smaller in the MEG than in EEG. Visible in EEG is that for Third 3, the GOF distribution is more diffuse compared to the other stimuli.

As the simulation studies have shown, dipole depth and amplitude are correlated. Therefore, Fig. 7.9 shows both the radial position on the x-axis and strength on the y-axis of the small stimuli relative to the full stimulus. An ideal result would be a relative position of 0 mm and, under the assumption that the cortical activations can be linearly added up, a relative strength of $\frac{1}{3}$. In the simulations, an increased patch radius led to a very small depth bias of the dipole scan, which would here show up as a positive depth shift of the small stimuli. Regarding the strength, the median across all small stimuli is indeed below 1, though especially in MEG there are several reconstruction results with over 50 % higher amplitudes. Notably, the case that the reconstructed dipole is stronger **and** more superficial (upper right quadrant of the plot) for a small stimulus than for the full stimulus does **not occur** for the EEG and only twice for the MEG.

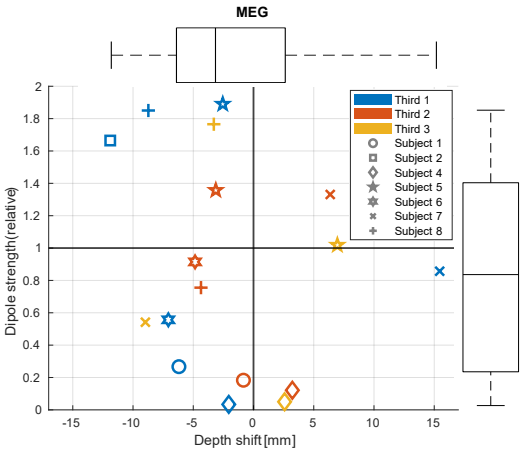

(a) Medians: depth: -3.1 (-6.4-2.7) mm, relative strength: 0.86 (0.25-1.43).

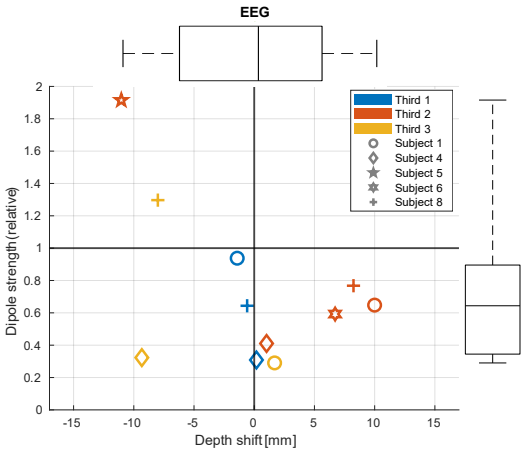

(b) Medians: depth: 0.2 (-6.4-5.5) mm, relative strength: 0.64 (0.34-0.90).

Figure 7.9: Depth shift (radial distance to the full stimulus) and relative amplitude of the reconstructed dipoles.

Due to the low GOF, not much data from Third 1 and Third 3 remains to be evaluated individually in a meaningful way. However, for Third 2, there remain 5 subjects with successful reconstructions from both EEG and MEG, so that the positions obtained by both can be compared. Figure 7.10 shows the distance between the reconstructed dipole from MEG and EEG. This distance is larger for the full stimulus (23 mm), than for the Third 2 stimulus (12 mm).

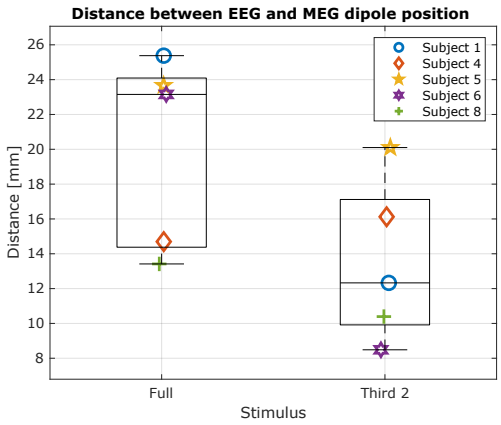

Figure 7.10: Distance between the reconstructed dipoles from MEG and EEG. Median values: Full: 23 (IQR 14-24), Third 2: 12 (IQR 10-17) mm.

7.3 Extent Estimation with IAS

As IAS, in contrast to the dipole scan, reconstructs an extended source distribution, the enforced ROI was chosen larger here, with a radius of 4 cm. For comparison with the simulations in Section 6.3, Fig. 7.11 shows the projected radius of the reconstruction for varying hyperprior tail length for subject 4. In the MEG, from a tail length of 8 dB onward, the three small stimuli are reconstructed with approximately the same extent (7.4 mm), and the full stimulus slightly larger (8.1 mm). For the EEG, the three small stimuli start out approximately the same (16.3 mm), with the full stimulus at 16.7 mm. For increasing tail length the radius for Third 2 becomes larger than for the full stimulus. The other two consistently remain lower.

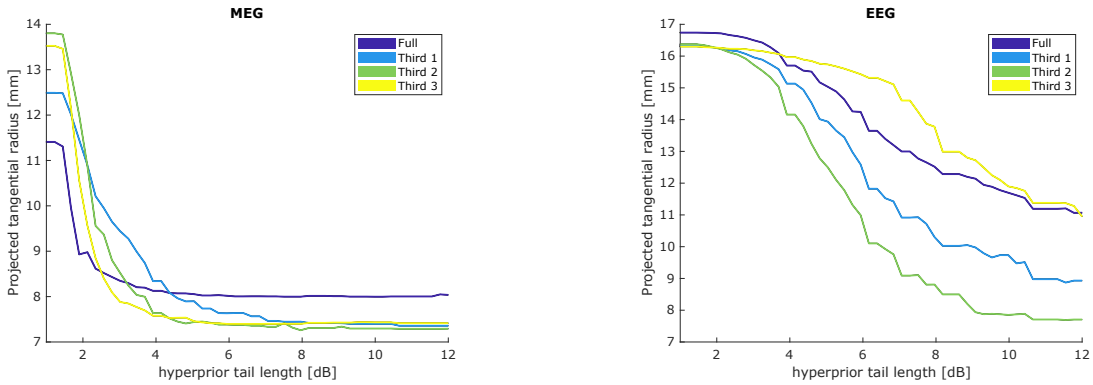

Figure 7.11: Projected radius for subject 4.

As the simulations have shown that there can be unstable results at <4 dB, while increasing the tail length much further may decrease the extent but does not further increase the GOF, a tail length of 6 dB was chosen to reconstruct all subject data for comparison. Figure 7.12 shows the GOF, which is overall similar to that achieved by the dipole scan. However, it is generally lower, with the medians for the full stimulus lying at 86 % and 82 % for MEG and EEG, while for the dipole scan they were 91 % and 93 %. As a consequence, the selection criterion to include results for further analysis was lowered to 65 %. This leads to a similar retained subset of the data as for the dipole scan, except notably, for subject 7 the IAS only achieves a GOF of 62 % even for the full stimulus.

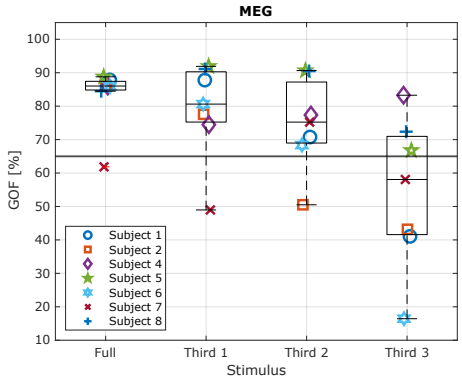

(a) Medians: Full: 86 (85-87), Third 1: 81 (75-90), Third 2: 75 (69-87), Third 3: 58 (42-71) %.

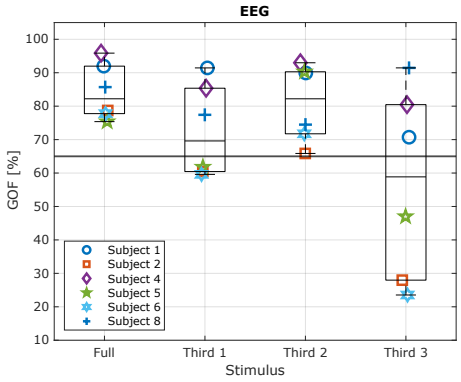

(b) Medians: Full: 82 (78-92), Third 1: 70 (60-85), Third 2: 82 (72-90), Third 3: 59 (28-80) %.

Figure 7.12: GOF for the IAS reconstruction of experimental data at 6 dB tail length, horizontal line marks 65 %.

As in Section 7.2, we will further examine the stimulus Third 2, for which the best reconstruction results were achieved. Figure 7.13 shows the projected radius for Third 2, relative to that of the full stimulus. In the EEG case, for all but one subject, the extent is smaller (median 0.93) for the smaller stimulus. However, for the MEG the median is actually higher (1.11).

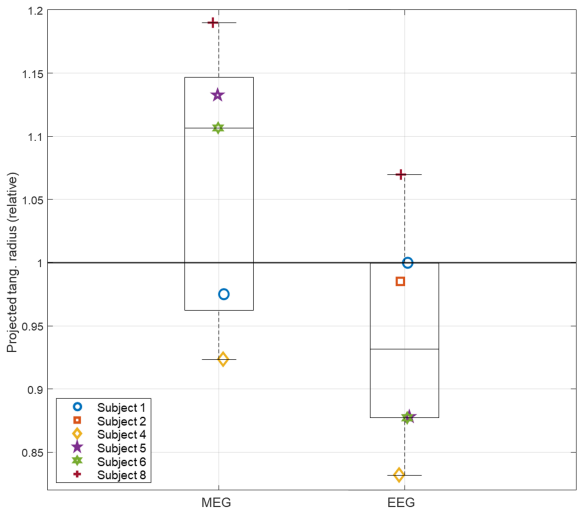

Figure 7.13: Radius (projected in tangential direction) of the reconstructed current density for stimulus Third 2 relative to full stimulus. Medians: MEG 1.11 (IQR 0.96-1.15), EEG 0.93 (0.88-1.00).

7.4 Discussion of Experimental Results

The experimental results show that not only the extent but also the position of the visual stimulus significantly effects the sensor-level and source-level results. In general, the full stimulus seems to be the more reliable paradigm, as it elicits a usable VER signal across all included participants. For the small stimuli, the quality of the VER measurement varies more strongly between subjects. However, the smaller stimuli do not, as one might expect, exhibit only a third of the SNR, but at least about 40 %. The fact that in some cases even a higher SNR is reached for Third 1 or Third 2 compared to the full stimulus seems physiologically unlikely, as the noise is assumed to be at a constant level throughout a measurement run, while the signal amplitude of the Thirds should be lower, even if it is unclear how much lower exactly. This phenomenon could be caused by a lower effective amplitude of the full stimulus due to canceling effects or due to more variability across trials. It could also be a property of using the GMFP to estimate SNR, as this is higher for focal signal peaks across a few sensors than for the same signal amplitude spread across several sensors. Alternatively, SNR can also be calculated per each channel or only for the channel with maximum amplitude.

The comparison of the topographies show that the sum of the individual signals from the three small stimuli is approximately equivalent to the response elicited directly by their combined area. However, they do not contribute equally to the full stimulus signal. Third 2, i.e., the middle stimulus/patch seems to contribute the strongest, which could also be caused by the other two partially canceling each other. However, Third 3 on its own exhibits a notably lower SNR across all participants. A strong radiality of the source could explain this drop for the MEG, but not for the EEG. The stimulus touches the midline of the visual field (vertical meridian): As explained in Section 2.2, this region is partially processed by both hemispheres. Considering the anatomy of the primary visual cortex, it is possible that the response to Third 3 is actually strongly tangential, but especially the tangential components cancel out from the mirrored two hemispheres. Therefore, SNR in VER experiments might be further increased by using a large stimulus but not letting it extend right up to the vertical meridian.

The GOF, unsurprisingly, follows the same trends as the SNR. It is evident that if the goal is to have good GOF across a range of participants, the full quadrant stimulus is the more reliable choice. However, for a few participants higher GOF was reached using smaller stimuli, especially Third 2. The fact that this only occurs for some participants could depend on the individual cortex anatomy. However, it has also been shown that attention modulates the VER, primarily later, more cognitive components, but also the first component: For this, di Russo et al. reports no statistically significant change in amplitude, but a significant latency lag of 7 ms in unattended vs attended condition [18]. A variance of latency due to changing attention over the course of the almost 10 min measurement per stimulus could also smear the averaged N75 peak and lower GOF.

The hypothesis that the extent can be estimated by the dipole strength can be confirmed only partially: The median dipole strengths are indeed lower for the small stimuli, but not 1/3 that of the 3 times larger stimulus, and there are also cases with higher amplitudes. The variance in position and strengths of the reconstructed dipoles is much larger than what has been observed in the simulations. Probably, this is caused by measurement noise and modeling errors, and more participants would be needed to see significant effects. Nevertheless, in the EEG, the median values fulfill the expectations from the simulations: The amplitude is lower and the position is slightly more superficial. Higher amplitudes could be explained by the dipoles being reconstructed too deep. However, in the simulations, a depth shift of 10 mm would correspond to a 5 % amplitude increase, whereas the experimentally observed changes are much larger (up to 200 %). Nevertheless, there is a systematic correlation between depth and amplitude, which is evident in the absence of dipoles that are simultaneously more superficial and have higher amplitude. This case would be difficult to interpret physically and physiologically.

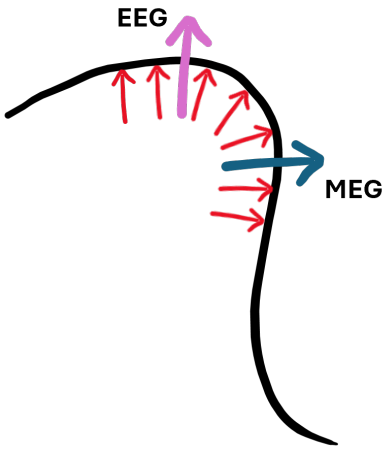

Figure 7.14: Oblique source patch (red), dipoles reconstructed by EEG/MEG will be biased towards components with radial/tangential orientation.

So far, results have mostly shown that due to the higher and more consistent SNR and GOF, using the larger stimulus is more beneficial. However, there is a crucial argument for using a small stimulus, particularly Third 2, the middle one. In many of the participants this stimulus still yielded good inverse results. And, notably, the distance between the MEG and EEG reconstructed dipoles was smaller for Third 2 than for the full stimulus. This is likely due to the contrary sensitivity to radial and tangential dipole moment components of the two modalities. As illustrated in Fig. 7.14, an oblique source which extends over a gyrus will have radial and tangential components. As the MEG is more sensitive to tangential components, the corresponding equivalent dipole will be reconstructed at the gyral wall, while the EEG, which is more sensitive to radial components, will yield a dipole at the gyrus crown. A smaller activated cortical patch should contain less variance in orientation, and therefore lead to a smaller distance between the MEG and EEG reconstructed dipoles.

This is an important advantage of using a reduced stimulus size, if the VER is to be used for calibration procedures as done with the somatosensory evoked response in [58]. In this technique, the MEG reconstructed dipole position is used to fix the position of the EEG dipole. Then, the conductivity value of the skull is optimized to maximize GOF for the EEG. The small-stimulus VER could provide an alternative paradigm for skull conductivity calibration, e.g., for subjects that do not want to be electrically stimulated as is necessary for the somatosensory evoked response, or to better estimate the conductivity in the occipital region.

The reconstructions obtained with IAS exhibit an overall lower GOF than the dipole scan results. This can be explained by the fact that the GOF is not the only property that is being optimized in IAS. Using dipole scanning, a consistently high GOF was achieved for the full quadrant stimulus for all subject data. The IAS reconstruction appears to fail here in the case of one subject, achieving a much lower GOF than the median. Although there is no clear explanation for why this happens, the reason probably relates to the measurement noise: For the full quadrant stimulus, the noise is the highest across participants in the case of that particular subject. It might be that the dipole scan somewhat overfits the noise thus achieving a high GOF, which the IAS aims to avoid by the use of priors. It is also possible that the algorithm did not find the global maximum of the posterior, possibly due to a non-optimal seed point or too few iterations.

Due to the contrasting results from EEG and MEG, no definite conclusion can be made on whether the IAS reconstruction can accurately reflect the extent of the underlying source. The estimated size for the activation elicited by the small stimulus is in median smaller for EEG but larger for MEG, compared to that of the full stimulus. An overestimation of the extent may be caused by the comparatively lower SNR. This could also explain the larger extent of Third 3 than the full stimulus in the example subject, as Third 3 exhibits particularly low SNR. Differences between MEG and EEG can often be related to their sensitivity to radial and tangential sources, however, without knowing the actual underlying source orientation, and how this affects the reconstructed extent, it is difficult to interpret these results.

8 Conclusion

In this thesis, the reconstruction of sources with varying spatial extent was investigated using simulated and experimental data. The localization error of extended source patches with (quasi-)radial dipole moments versus single dipole sources was shown to be a systematic, but negligible bias to deeper positions. This error increases for curved patches versus planar patches. The IAS inverse method is capable of reconstructing current distributions whose spread reflects the size of the underlying source patch. However, using cortex-normal dipoles, i.e., allowing unsymmetrical position and orientation distributions within a patch, leads to unsystematic reconstruction results with regard to the reference source radius.

In the real VER experiments, it became evident that stimulus size is not the only factor influencing the sensor-level measurements and their inverse analysis. The three stimuli of same size but different angular positions within the lower right quadrant of the visual field varied in SNR and GOF: The middle stimulus (Third 2) exhibited the highest SNR and GOF, the stimulus just below the horizontal meridian (Third 1) the second highest, and the lower stimulus next to the vertical meridian (Third 3) the lowest. It could not be empirically confirmed that the larger source extent associated with the full quadrant stimulus leads to a systematic mislocalization of the source. Rather, it led to higher SNR and more consistent results across participants. Especially for Third 3, SNR was often insufficient for inverse analysis. However, for Third 2, reliable reconstructions were achieved for most participants. It could be shown that for this stimulus, the distance between the EEG and MEG-obtained dipoles was smaller than for the full quadrant stimulus.

Arguably, the patches used in the simulations do not accurately model the real source configurations: The experimentally obtained EMEG topographies already show that the sources clearly vary in net dipole moment orientation due to the local cortex anatomy. This is one factor that makes it difficult to relate the systematic differences in position or distribution spread found in the simulations to the real VER data. Additionally, the effects are of such small magnitude with respect to the variances caused by noise, that a larger sample size may be necessary to reproduce them.

All in all, the larger stimulus, encompassing a whole quadrant of the visual field, is a good choice for consistently obtaining usable VER data, and allows for accurate dipole localization. However, the stimulus should not extend right up to the vertical meridian of the visual field. In some cases, sufficient SNR can be achieved for a smaller stimulus, which is more likely if the stimulus lies in the middle of the quadrant. Then, it is beneficial to use the smaller stimulus in combined MEG and EEG studies, as the distance between the dipoles reconstructed from the respective data is decreased. This is crucial, especially if the VER is to be used for conductivity calibration.

The observed discrepancy between the MEG and EEG also underlines the importance of using both modalities in clinical applications, where MEG is still underrepresented: The distance between the MEG and EEG-reconstructed dipoles can serve as an addi-

tional parameter to gauge the size of, e.g., an extended epileptogenic zone. Source strength alone may not always be a reliable indicator, due to canceling effects decreasing the amplitude for larger patches. In cases where the discrepancy between MEG and EEG is large, also both are needed to correctly estimate the center of the activity.

In future studies, the curvature of the patch could be implemented as a variable parameter additional to the radius. This would allow modeling more realistic sources located at gyrus crowns and sulcal valleys, while still maintaining a controllable scenario. Empirically, the VER may be improved by placing a small stimulus in the middle of a visual quadrant and continuously increasing its size. Thereby, an optimal extent for high SNR and simultaneous high spatial accuracy could be found.

Bibliography

[1] Z. Akalin Acar, C. E. Acar, and S. Makeig. "Simultaneous head tissue conductivity and EEG source location estimation". In: *NeuroImage* 124 (2016), 168–180. DOI: 10.1016/j.neuroimage.2015.08.032.

[2] J. M. Ales, J. L. Yates, and A. M. Norcia. "On determining the intracranial sources of visual evoked potentials from scalp topography: A reply to Kelly et al. (this issue)". In: *NeuroImage* 64 (2013), 703–711. DOI: 10.1016/j.neuroimage.2012.09.009.

[3] J. M. Ales, J. L. Yates, and A. M. Norcia. "V1 is not uniquely identified by polarity reversals of responses to upper and lower visual field stimuli". In: *NeuroImage* 52.4 (2010), 1401–1409. DOI: 10.1016/j.neuroimage.2010.05.016.

[4] American Clinical Neurophysiology Society. "Guideline 5: Guidelines for Standard Electrode Position Nomenclature". In: *Journal of Clinical Neurophysiology* 23.2 (2006), 107–110. DOI: 10.1097/00004691-200604000-00006.

[5] M. Antonakakis et al. "Targeted and optimized multi-channel transcranial direct current stimulation for focal epilepsy: An N-of-1 trial". In: *Brain Stimulation* 17.2 (2024), 221–223. DOI: 10.1016/j.brs.2024.02.010.

[6] T. Bast et al. "EEG and MEG Source Analysis of Single and Averaged Interictal Spikes Reveals Intrinsic Epileptogenicity in Focal Cortical Dysplasia". In: *Epilepsia* 45.6 (2004), 621–631. DOI: 10.1111/j.0013-9580.2004.56503.x.

[7] B. L. Beard, D. M. Levi, and S. A. Klein. "Vernier acuity with non-simultaneous targets: The cortical magnification factor estimated by psychophysics". In: *Vision Research* 37.3 (1997), 325–346. DOI: 10.1016/S0042-6989(96)00109-5.

[8] M. Brigell et al. "Guidelines for calibration of stimulus and recording parameters used in clinical electrophysiology of vision". In: *Documenta Ophthalmologica* 107 (2003), 185–193. DOI: 10.1023/a:1026244901657.

[9] H. Buchner et al. "Inverse localization of electric dipole current sources in finite element models of the human head". In: *Electroencephalography and clinical Neurophysiology* 102 (1997), 278. DOI: 10.1016/S0013-4694(96)95698-9.

[10] D. Calvetti and E. Somersalo. "A Gaussian hypermodel to recover blocky objects". In: *Inverse Problems* 23.2 (2007), 733. DOI: 10.1088/0266-5611/23/2/016.

[11] D. Calvetti et al. "Conditionally gaussian hypermodels for cerebral source localization". In: *SIAM Journal on Imaging Sciences* 2.3 (2009), 879–909. DOI: 10.1137/080723995.

[12] A. Capilla et al. "Retinotopic mapping of visual event-related potentials". In: *Biological Psychology* 118 (2016), 114–125. DOI: 10.1016/j.biopsycho.2016.05.009.

[13] D. Cohen and B. Cuffin. "Demonstration of useful differences between magnetoencephalogram and electroencephalogram". In: *Electroencephalography and Clinical Neurophysiology* 56.1 (1983), 38–51. DOI: 10.1016/0013-4694(83)90005-6.

[14] C. E. Collins et al. “Cortical cell and neuron density estimates in one chimpanzee hemisphere”. In: *Proceedings of the National Academy of Sciences* 113.3 (2016), 740–745. DOI: 10.1073/pnas.1524208113.

[15] B. Cuffin et al. “Experimental tests of EEG source localization accuracy in spherical head models”. In: *Clinical Neurophysiology* 112.1 (2001), 46–51. DOI: 10.1016/S1388-2457(00)00488-0.

[16] G. D. Dawson. “A Summation Technique for the Detection of Small Evoked Potentials”. In: *Electroencephalography and Clinical Neurophysiology* 6 (1954), 65–84. DOI: 10.1016/0013-4694(54)90007-3.

[17] J. DeFelipe and I. Fariñas. “The pyramidal neuron of the cerebral cortex: Morphological and chemical characteristics of the synaptic inputs”. In: *Progress in Neurobiology* 39.6 (1992), 563–607. DOI: 10.1016/0301-0082(92)90015-7.

[18] F. Di Russo and D. Spinelli. “Electrophysiological evidence for an early attentional mechanism in visual processing in humans”. In: *Vision Research* 39.18 (1999), 2975–2985. DOI: 10.1016/S0042-6989(99)00031-0.

[19] F. Di Russo et al. “Cortical sources of the early components of the visual evoked potential”. In: *Human Brain Mapping* 15.2 (2002), 95–111. DOI: 10.1002/hbm.10010.

[20] S. A. Engel, G. H. Glover, and B. A. Wandell. “Retinotopic Organization in Human Visual Cortex and the Spatial Precision of Functional MRI”. In: *Cerebral Cortex* 7.2 (1997), 181–192. DOI: 10.1093/cercor/7.2.181.

[21] M. Fahimi Hnazaee et al. “Localization of deep brain activity with scalp and subdural EEG”. In: *NeuroImage* 223 (2020), 117344. DOI: 10.1016/j.neuroimage.2020.117344.

[22] D. J. Felleman and D. C. Van Essen. “Distributed Hierarchical Processing in the Primate Cerebral Cortex”. In: *Cerebral Cortex* 1.1 (1991), 1–47. DOI: 10.1093/cercor/1.1.1-a.

[23] M. Fuchs et al. “Linear and nonlinear current density reconstructions”. In: *Journal of clinical Neurophysiology* 16.3 (1999), 267–295. DOI: 10.1097/00004691-199905000-00006.

[24] F. Galaz Prieto et al. “Multi-compartment head modeling in EEG: Unstructured boundary-fitted tetra meshing with subcortical structures”. In: *PLOS ONE* 18.9 (2023), 1–25. DOI: 10.1371/journal.pone.0290715.

[25] J. Gross, M. Junghöfer, and C. Wolters. “Bioelectromagnetism in Human Brain Research: New Applications, New Questions”. In: *The Neuroscientist* 29.1 (2023), 62–77. DOI: 10.1177/10738584211054742.

[26] M. Hämäläinen et al. “Magnetoencephalography—theory, instrumentation, and applications to noninvasive studies of the working human brain”. In: *Rev. Mod. Phys.* 65.2 (1993), 413–497. DOI: 10.1103/RevModPhys.65.413.

[27] R. Hari et al. “Evoked and Event-Related Responses”. In: *MEG-EEG Primer*. Oxford University Press, Mar. 2017. DOI: 10.1093/med/9780190497774.003.0011.

[28] H. von Helmholtz. “Ueber einige Gesetze der Vertheilung elektrischer Ströme in körperlichen Leitern mit Anwendung auf die thierisch-elektrischen Versuche”. In: *Annalen der Physik* 165.7 (1853), 353–377. DOI: 10.1002/andp.18531650603.

[29] M. B. Höltershinken et al. “The Local Subtraction Approach for EEG and MEG Forward Modeling”. In: *SIAM Journal on Scientific Computing* 47.1 (2025), B160–B189. DOI: 10.1137/23M1582874.

[30] J. C. Horton and W. F. Hoyt. “The representation of the visual field in human striate cortex: a revision of the classic Holmes map”. In: *Archives of ophthalmology* 109.6 (1991), 816–824. DOI: 10.1001/archopht.1991.01080060080030.

[31] A. Huber and D. Kömpf. *Klinische Neuroophthalmologie*. Thieme, 1998. ISBN: 3131035617.

[32] S. P. Kelly, C. E. Schroeder, and E. C. Lalor. “What does polarity inversion of extrastriate activity tell us about striate contributions to the early VEP? A comment on Ales et al. (2010)”. In: *NeuroImage* 76 (2013), 442–445. DOI: 10.1016/j.neuroimage.2012.03.081.

[33] S. P. Kelly et al. “The cruciform model of striate generation of the early VEP, re-illustrated, not revoked: A reply to Ales et al. (2013)”. In: *NeuroImage* 82 (2013), 154–159. DOI: 10.1016/j.neuroimage.2013.05.112.

[34] T. R. Knösche and J. Haueisen. *EEG/MEG Source Reconstruction: Textbook for Electro-and Magnetoencephalography*. Springer International Publishing, 2022. DOI: 10.1007/978-3-030-74918-7.

[35] K. Kobayashi et al. “Dipole Modeling of Epileptic Spikes Can Be Accurate or Misleading”. In: *Epilepsia* 46.3 (2005), 397–408. DOI: 10.1111/j.0013-9580.2005.31404.x.

[36] D. Kordek et al. “Effect of Dioptric Blur on Pattern-Reversal and Motion-Onset VEPs as Used in Clinical Research”. In: *Translational Vision Science & Technology* 11.12 (2022), 7. DOI: 10.1167/tvst.11.12.7.

[37] P. Krolak-Salmon et al. “Human lateral geniculate nucleus and visual cortex respond to screen flicker”. In: *Annals of Neurology* 53.1 (2003), 73–80. DOI: 10.1002/ana.10403.

[38] F.-H. Lin et al. “Assessing and improving the spatial accuracy in MEG source localization by depth-weighted minimum-norm estimates”. In: *NeuroImage* 31.1 (2006), 160–171. DOI: 10.1016/j.neuroimage.2005.11.054.

[39] F. Lucka et al. “Hierarchical Bayesian inference for the EEG inverse problem using realistic FE head models: Depth localization and source separation for focal primary currents”. In: *NeuroImage* 61.4 (2012), 1364–1382. DOI: 10.1016/j.neuroimage.2012.04.017.

[40] T. Medani et al. “FEM method for the EEG forward problem and improvement based on modification of the Saint Venant’s method”. In: *Progress in Electromagnetics Research* 153 (2015), 11–22. DOI: 10.2528/PIER15050102.

[41] N. Mikuni et al. “Simultaneous Recording of Epileptiform Discharges by MEG and Subdural Electrodes in Temporal Lobe Epilepsy”. In: *NeuroImage* 5.4 (1997), 298–306. DOI: 10.1006/nimg.1997.0272.

[42] J. Mosher and R. Leahy. “Recursive MUSIC: A framework for EEG and MEG source localization”. In: *IEEE Transactions on Biomedical Engineering* 45.11 (1998), 1342–1354. DOI: 10.1109/10.725331.

[43] J. C. de Munck. “The potential distribution in a layered anisotropic spheroidal volume conductor”. In: *Journal of Applied Physics* 64.2 (1988), 464–470. DOI: 10.1063/1.341983.

[44] J. C. D. Munck, B. W. V. Dijk, and H. Spekreijse. “Mathematical Dipoles are Adequate to Describe Generators of Human Brain Activity”. In: *IEEE Transactions on Biomedical Engineering* 35.11 (1988), 960–966. DOI: 10.1109/10.8677.

[45] S. Murakami and Y. Okada. “Contributions of principal neocortical neurons to magnetoencephalography and electroencephalography signals”. In: *Journal of Physiology* 575.3 (2006), 925–936. DOI: 10.1113/jphysiol.2006.105379.

[46] A. Nüßing. “Fitted and Unfitted Finite Element Methods for Solving the EEG Forward Problem”. Dissertation. University of Münster, 2018.

[47] J. V. Odom et al. “ISCEV standard for clinical visual evoked potentials: (2016 update)”. In: *Documenta Ophthalmologica* 133.1 (2016), 1–9. DOI: 10.1007/s10633-016-9553-y.

[48] R. D. Pascual-Marqui. “Standardized low-resolution brain electromagnetic tomography (sLORETA): technical details.” In: *Methods and findings in experimental and clinical pharmacology* 24 Suppl D (2002), 5–12.

[49] M. C. Piastra et al. “A comprehensive study on electroencephalography and magnetoencephalography sensitivity to cortical and subcortical sources”. In: *Human Brain Mapping* 42.4 (2021), 978–992. DOI: 10.1002/hbm.25272.

[50] F. Pizzo et al. “Deep brain activities can be detected with magnetoencephalography”. In: *Nature Communications* 10.1 (2019), 971. DOI: 10.1038/s41467-019-08665-5.

[51] T. Popov, R. Oostenveld, and J. M. Schoffelen. “FieldTrip Made Easy: An Analysis Protocol for Group Analysis of the Auditory Steady State Brain Response in Time, Frequency, and Space”. In: *Frontiers in Neuroscience* 12 (2018), 711. DOI: 10.3389/fnins.2018.00711.

[52] A. Qiu et al. “Estimating linear cortical magnification in human primary visual cortex via dynamic programming”. In: *NeuroImage* 31.1 (2006), 125–138. DOI: 10.1016/j.neuroimage.2005.11.049.

[53] S. Rampp et al. “Magnetoencephalography for epileptic focus localization in a series of 1000 cases”. In: *Brain* 142.10 (2019), 3059–3071. DOI: 10.1093/brain/awz281.

[54] A. Rezaei et al. “Parametrizing the Conditionally Gaussian Prior Model for Source Localization with Reference to the P20/N20 Component of Median Nerve SEP/SEF”. In: *Brain Sciences* 10.12 (2020), 1–22. DOI: 10.3390/brainsci10120934.

[55] B. J. Roth et al. “How well does a three-sphere model predict positions of dipoles in a realistically shaped head?” In: *Electroencephalography and Clinical Neurophysiology* 87.4 (1993), 175–184. DOI: 10.1016/0013-4694(93)90017-P.

[56] L. Rutz. “Vergleich enzephalographischer Verfahren (MEG, EEG) und Quellenanalysen von visuell evozierten Antworten”. Bachelor’s Thesis. University of Münster, 2022.

[57] J. Sarvas. “Basic mathematical and electromagnetic concepts of the biomagnetic inverse problem”. In: *Physics in Medicine & Biology* 32.1 (1987), 11. DOI: 10.1088/0031-9155/32/1/004.

[58] S. Schrader et al. “A novel method for calibrating head models to account for variability in conductivity and its evaluation in a sphere model”. In: *Physics in Medicine and Biology* 65.24 (2020), 245043. DOI: 10.1088/1361-6560/abc5aa.

[59] M. I. Sereno et al. “Borders of Multiple Visual Areas in Humans Revealed by Functional Magnetic Resonance Imaging”. In: *Science* 268.5212 (1995), 889–893. DOI: 10.1126/science.7754376.

[60] R. Sinha et al. “Cellular and Circuit Mechanisms Shaping the Perceptual Properties of the Primate Fovea”. In: *Cell* 168.3 (2017), 413–426. DOI: 10.1016/j.cell.2017.01.005.

[61] S. D. Slotnick et al. “Electrophysiological estimate of human cortical magnification”. In: *Clinical Neurophysiology* 112.7 (2001), 1349–1356. DOI: 10.1016/S1388-2457(01)00561-2.

[62] B. J. Thio and W. M. Grill. “Relative contributions of different neural sources to the EEG”. In: *NeuroImage* 275 (2023), 120179. DOI: 10.1016/j.neuroimage.2023.120179.

[63] J. Vorwerk et al. “A guideline for head volume conductor modeling in EEG and MEG”. In: *NeuroImage* 100 (2014), 590–607. DOI: 10.1016/j.neuroimage.2014.06.040.

[64] J. Vorwerk et al. “Influence of Head Tissue Conductivity Uncertainties on EEG Dipole Reconstruction”. In: *Frontiers in Neuroscience* 13 (2019), 531. DOI: 10.3389/fnins.2019.00531.

[65] C. H. Wolters et al. “Numerical Mathematics of the Subtraction Method for the Modeling of a Current Dipole in EEG Source Reconstruction Using Finite Element Head Models”. In: *SIAM Journal on Scientific Computing* 30.1 (2008), 24–45. DOI: 10.1137/060659053.

[66] C. Wolters, L. Grasedyck, and W. Hackbusch. "Efficient Computation of lead field bases and influence matrix for the FEM-based EEG and MEG inverse problem". In: *Inverse Problems* 20.4 (2004), 1099–1116. DOI: 10.1088/0266-5611/20/4/007.

[67] C. Wolters et al. "Geometry-adapted hexahedral meshes improve accuracy of finite-element- method-based EEG source analysis". In: *IEEE Transactions on Biomedical Engineering* 54.8 (2007), 1446–1453. DOI: 10.1109/TBME.2007.890736.

Software References

[68] J. P. Ahrens, B. Geveci, and C. C. Law. "ParaView: An End-User Tool for Large-Data Visualization". In: *The Visualization Handbook*. 2005. DOI: 10.1016/B978-012387582-2/50038-1.

[69] D. H. Brainard. "The Psychophysics Toolbox". In: *Spatial Vision* 10.4 (1997), 434–436. DOI: 10.1163/156856897X00357.

[70] T. Erdbrügger et al. *The University of Münster DUNEuro-based pipeline to create personalized head models with calibrated skull conductivity for EEG/MEG source analysis and optimized multi-channel tES*. Zenodo. 2024. DOI: 10.5281/zenodo.13789178.

[71] K. J. Friston et al. "Statistical parametric maps in functional imaging: A general linear approach". In: *Human Brain Mapping* 2.4 (1994), 189–210. DOI: 10.1002/hbm.460020402.

[72] C. Gaser et al. "CAT: A computational anatomy toolbox for the analysis of structural MRI data". In: *GigaScience* 13 (2024). DOI: 10.1093/gigascience/giae049.

[73] Q. He, A. Rezaei, and S. Pursiainen. "Zeffiro User Interface for Electromagnetic Brain Imaging: a GPU Accelerated FEM Tool for Forward and Inverse Computations in Matlab". In: *Neuroinformatics* 18.2 (2020), 237–250. DOI: 10.1007/s12021-019-09436-9.

[74] M. Jenkinson et al. "Improved Optimization for the Robust and Accurate Linear Registration and Motion Correction of Brain Images". In: *NeuroImage* 17.2 (2002), 825–841. DOI: 10.1006/nimg.2002.1132.

[75] J. V. Manjón et al. "Adaptive non-local means denoising of MR images with spatially varying noise levels". In: *Journal of Magnetic Resonance Imaging* 31.1 (2010), 192–203. DOI: 10.1002/jmri.22003.

[76] J. Mazziotta et al. "A probabilistic atlas and reference system for the human brain: International Consortium for Brain Mapping (ICBM)". In: *Philosophical Transactions of the Royal Society of London. Series B: Biological Sciences* 356.1412 (2001), 1293–1322. DOI: 10.1098/rstb.2001.0915.

[77] R. Oostenveld et al. “FieldTrip: Open source software for advanced analysis of MEG, EEG, and invasive electrophysiological data”. In: *Computational Intelligence and Neuroscience* 2011 (2011), 156869. DOI: 10.1155/2011/156869.

[78] S. Schrader et al. “DUNEuro - A software toolbox for forward modeling in bioelectromagnetism”. In: *PLoS ONE* 16.6 (2021), e0252431. DOI: 10.1371/journal.pone.0252431.

[79] A. Semechko. *Suite of Functions to Perform Uniform Sampling of a Sphere*. GitHub. 2019. URL: https://github.com/AntonSemechko/S2-Sampling-Toolbox (visited on 11/27/2024).

[80] SimBio Development Group. *SimBio: A generic environment for bio-numerical simulations*. URL: https://www.mrt.uni-jena.de/simbio (visited on 11/29/2024).

[81] F. Tadel et al. “Brainstorm: A User-Friendly Application for MEG/EEG Analysis”. In: *Computational Intelligence and Neuroscience* 2011.1 (2011), 879716. DOI: 10.1155/2011/879716.

Illustration Sources

[82] O. Colomés et al. “Elements and shape functions”. In: *Finite Elements in Civil Engineering and Geosciences*. Delft University of Technology, 2023. URL: https://teachbooks.tudelft.nl/computational-modelling (visited on 01/28/2025).

[83] Wikimedia Commons. *Retinotopic organization*. 2015. URL: https://de.m.wikipedia.org/wiki/Datei:Retinotopic_organization.png (visited on 03/11/2025).